

Numerical simulation of the dust flux on a spacecraft in orbit around an aspherical cometary nucleus – I

M. Fulle¹, J.F. Crifo², and A.V. Rodionov³

¹ Osservatorio Astronomico di Trieste, Via Tiepolo 11, I-34131 Trieste, Italy (fulle@ebe.oat.ts.astro.it)

² CNRS, Service d'Aéronomie, B.P.3, F-91371 Verrières-le-Buisson Cedex, France (crifo@aerov.jussieu.fr)

³ Central Research Institute on Machine Building (TsNIIMASch), Pyonierskaya 4, Korolev, Moscow Region 141070, Russia

Received 26 November 1998 / Accepted 25 March 1999

Abstract. This study is the first investigation of the dust collection by a spacecraft orbiting a cometary nucleus, which is based on a physically consistent ab-initio model of the dust distribution in the vicinity of an aspherical comet nucleus. The homogeneous bean-shaped nucleus of Crifo & Rodionov (1997a) is used, with updated parameter values adapted to comet 46P/Wirtanen, target of the Rosetta mission, but the conclusions of the study have a general significance. The near-nucleus dust distribution is computed from the dusty gasdynamic model of the above reference, except that a power-law size distribution with differential exponent $\alpha = -3.5$ is used here. The more distant distribution is computed from a Keplerian fountain model. Dust flux and fluences are evaluated for surfaces with various orientations, taking or not into account flux collimation, so that both the signal from dust analysers and the spacecraft contamination can be assessed. The results are compared to previous evaluations based either on the unphysical, spherically symmetric coma assumption, or on the highly asymmetric “effective nucleus dust source” derived from the Giotto Halley flyby in-situ dust measurements by Fulle et al. (1995), scaled appropriately to the present problem. The main results are the following: (1) The results based on the spherical assumption can at best be used for a global (benchmark) test of the correctness of a more realistic models, but otherwise do not represent the fluxes or fluences undergone by any spacecraft surface during any realistic sequence of spacecraft orbits; (2) there is a strong difference between the results from the present model, and those based on Fulle et al. (1995), due in part to the fact that the present dust source is less anisotropic than the “effective” source derived there; the two evaluations thus provide for the first time an estimate of the prediction uncertainties associated with the absence of a precise knowledge of the nucleus shape; (3) other differences between the present and previous results are due to the non-radiality of the near-nucleus motion, and to the total absence of a biunivocal mass-terminal velocity relation in the present model; (4) the “reflected” component of grains returned towards the nucleus by radiation pressure appears particularly sensitive to the dust ejection model, and is therefore a potentially important quantity to measure, to constrain such models; (5) the strongest dust irra-

diation is generally obtained for orbits located in the dawn–dusk meridian; (6) proper allowance for the non-radial near-nucleus dust motion is extremely critical to the strategy of dust fluence reduction on critical spacecraft systems.

Key words: comets: general – comets: individual: 46P/Wirtanen

1. Introduction

During the first decade of the XXIst century, several spacecrafts will be flown by, or inserted in orbit around, an active cometary nucleus¹. Some of them will carry instruments dedicated to the in-situ study of the dust properties, and all of them will be submitted to dust impacts, which represents various kinds of hazards.

To our knowledge, the forecasting of the levels of dust collection by spacecrafts in a coma has hitherto been done on the basis of utterly simplified assumptions with respect to the distribution of dust in the vicinity of the nucleus. In general a fictitious 1-D spherically symmetric nucleus is assumed, having the assumed total gas and dust production rate of the real comet. This is perhaps acceptable when dealing with large distances to the nucleus, where the dust coma is not too aspherical. But close to the nucleus numerical simulations predict that the dust coma will be extremely inhomogeneous (Crifo & Rodionov, 1997a,b). It is sometimes argued, however, that, due to the conservation of the dust mass flux, if a spacecraft scans a closed surface S encircling the nucleus, then “owing to some kind of Gauss theorem”, its fluence will be independent from the details of the dust distribution, and therefore can most simply be evaluated using the 1-D model. This is unwarranted: in general, the flu-

¹ The NASA mission DS1 will in 2001 fly by comets Wilson Harrington (a “defunct” comet!) and P/Borrelly; the NASA mission “Stardust” will return dust grains collected in 2004 in the coma of comet Wild-2; the NASA mission “Comtour” will fly by comets Encke in 2003, Schwachmann-Wachmann III in 2006, and d’Arrest in 2009, the NASA mission DS4 will orbit and land on comet Tempel III in 2003, and finally the ESA mission “Rosetta” will orbit and land on comet P/Wirtanen in 2013.

ence relative to a spacecraft element is *not* equal to the dust flux across S , since the normal to S does *not* in general enter into the definition of the fluence. Furthermore, the spacecraft does not scan S uniformly in time. And finally it is unlikely that a spacecraft orbiting a nucleus will ever scan a *closed* surface around it. Thus, we do expect that the integrated dust flux will strongly depend upon the exact dust distribution in the coma. And this raises the question (absent in a 1-D approach) of how to minimize or maximize this integrated flux (in general, for technical reasons, one wants to minimize the fluence, but dust analysis experiments may just ask for the opposite!). Furthermore, not only the time-integrated fluence may matter, but, as well, its time variation, which again depends on the real spatial dust distribution. Also, the 1-D model has the peculiarity that the dust motion is strictly radial, which is not the case in a real dust coma close to the nucleus surface (Crifo & Rodionov, 1997a,b, 1998a,b). It is evident that a spacecraft surface oriented radially will receive a null fluence in a 1-D model, but not in a real case. For the same reason, when a dust detector with a small field of view is considered, the accumulated signal predicted by the 1-D model cannot be in general correct. A final, and difficult problem is that of relating the size distribution of the collected dust to the size distribution of that emitted by the nucleus. Whether or not the spacecraft scans a closed surface, the two distributions will differ, because of the complicated dust dynamics around a real nucleus (see Fulle et al., 1995). And again, the question might be raised of which orbits and which collection directions will minimize this difference.

The first investigation of the dust impacts in a non-uniform coma was done by Fulle et al. (1997) (hereafter designated as ‘F97’) who analysed the sensitivity of the “Rosetta” orbiter dust analyzer “Giada” (Bussoletti et al., 1998) assuming an empirical dust environment, based on a previous fit to the “Didsy” Halley flyby dust impact detector (McDonnell et al. 1987, Fulle et al. 1995). They found that, as expected, the dust collection essentially depends on the environment anisotropy, when one assumes arbitrarily oriented probe orbits. However, while they considered orbits very close to the nucleus surface, their model dust distribution was a purely mathematical extrapolation from data acquired at thousands of kilometers away from the nucleus of P/Halley, and therefore was independent from the nucleus size, shape, topography and spin evolution. It is clear, however, that the dust environment *close to a nucleus surface* must be dependent upon these nucleus characteristics (Crifo & Rodionov, 1997a,b). In fact, the description of this environment should, in addition, be based on a realistic representation of the dust itself, since, close to the nucleus surface, the dust dynamics is critically dependent upon characteristics of the dust (in first place the dust grain shape) that are currently ignored (see Crifo & Rodionov, 1999a,b). Thus, a rigorous approach must consist of (1) establishing a plausible nucleus physical model and a plausible dust physical model; (2) assuming a realistic nucleus spin state; (3) computing the gas and dust environment of the nucleus as a function of time, using a 3-D gasdynamic model, up to the upper boundary of the gas-dust interaction region; (4) extrapolating the dust distribution at any greater distance, using

rigorous Keplerian dynamics – this last step is needed, because gasdynamic models do not take into account the radiation pressure force, nor the differential Keplerian motion of the dust and nucleus; in particular, gasdynamic models cannot yield any information on the “reflected” component of those grains which have been returned towards the nucleus vicinity by the solar radiation pressure; (5) finally, computing the dust flux collected by the probe, taking into account the characteristics of its orbit. This is surely an enormous task, which however begins to be faced.

This paper is a first step in this direction. We still retain an unrealistic dust model (spherical grains). We neglect the nucleus rotation, as well as its orbital motion. Also, we adopt the simplest possible nucleus activity model, i.e. pure surface sublimation of H_2O (excluding, for instance, distributed gas and dust production). On the other hand, we consider a nucleus with an aspherical shape, specifically the “bean” shape defined in Crifo & Rodionov (1997b). We adopt model parameters adapted to the future ESA mission “Rosetta” to Comet 46P/Wirtanen (Bar-Nun et al. 1993), but the results are qualitatively applicable to any other similar mission. The very small nucleus size (0.6 km equivalent radius) of 46P/Wirtanen suggested by the recent observations of Lamy et al. (1998), and its relatively high activity at perihelion ($1-3 \times 10^{28}$ molecule per second) suggest that most of its surface must be active (unless distributed production of H_2O is at play, which surely cannot be excluded in principle, but which is excluded here for the sake of simplicity, as mentioned above); thus, as in Crifo & Rodionov (1997b), we assume the nucleus surface to be homogeneous in composition. In spite of its simplicity, this nucleus generates a fairly inhomogeneous dust coma, and is therefore quite fit to our present objective.

The assumptions that the nucleus orientation is fixed in space, and that it stays permanently at its perihelion, are strong assumptions, since the orbital period of the probe around the nucleus may reach a month, thus is surely much longer than the nucleus spin period, and may be long enough that the sun-comet distance will change significantly during a single probe orbital revolution. Furthermore, the acceleration time (by gas drag) of the largest ejectable grains may itself exceed the nucleus spin period, so that the distribution of those large grains may not be realistically represented by a stationary model. In this paper, we are forced to neglect these effects: taking into account them will be the next steps of our simulations, which however will imply an enormous increase both in the number of model parameters (to represent the nucleus spin, now totally undetermined, and the heliocentric dependence of the comet activity, poorly constrained by observations), and in computer memory and CPU time. Still, the problem of the unrealistic representation of the dust will persist. Introducing a dispersion (at any fixed grain mass) in grain shape and specific mass would surely result in a dispersion in terminal grain velocity vector. It is clear however that the advancement towards a fully realistic model can only be made by steps.

Since most of the physical characteristics of the target comet 46P/Wirtanen will remain unknown until the “Rosetta” probe will reach it, one can only sample the full range of probable

values of the required model parameters, and search for general characteristics of the collected dust flux. In this respect, the simulations presented in this paper can be considered to correspond to the (improbable) case of a non rotating nucleus (or with a very long spin period) and of a comet showing slow activity changes close to perihelion. In any case, the comparison of the results of this paper with those provided by F97, based on a totally different anisotropic dust environment, and with the isotropic model, already will let us identify some general characteristics of the collected dust flux. Particular attention will be paid to the dependence of the dust flux upon the probe orbital parameters, such as the probe orbit orientation with respect to a nucleus–attached reference system, and the probe orbiting distance from the nucleus center.

The comparison between the results provided by the two anisotropic dust environments (F97 and this paper) allows us to quantify the contribution to the dust flux of the previously mentioned reflected grains. In isotropic comae, the direct flux is always much larger than the reflected one, but in anisotropic comae the reflected flux may be larger, for some probe orbits, than the direct one. The degree of coma anisotropy assumed in F97 (on heuristic grounds) was rather strong, compared to that exhibited by the present model (where the anisotropy is mostly due to the fact that the homogeneous nucleus considered is inactive during the night). Thus, the comparison of the results is indicative of the probable range of relative contribution of the reflected and direct dust populations. Finally, the comparison between the results of this paper with those from an isotropic model allows us to point out which characteristics of the dust fluence cannot be revealed by such simplistic isotropic models. This is of course essential in defining safe probe orbiting strategies.

2. The model

2.1. The nucleus, and its gas and dust emission

We assume that 46P/Wirtanen nucleus has the “bean” shape defined in Crifo & Rodionov (1997b) – more precisely, the most concave one considered there, which has a concavity parameter $h = 0.8$. This shape is shown on Fig. 1. In order to be more consistent with the recent observations of Lamy et al. (1998) of comet 46P/Wirtanen, a new (reduced) value of the nucleus characteristic size $R_n = 750$ m is adopted here. At each sunlit point of the surface, a sublimation energy budget equation is written, and the whole set of these budget equations is solved consistently with the gas and dust outflow Euler equations, up to an outer boundary where free outflow conditions are assumed. The “surface icy area fraction” f (which characterizes the relative abundance of ice and refractory dust at each point of the surface) is set to the constant value 0.9, ensuring a perihelion H_2O production rate $Q = 1.2 \times 10^{28}$ molecule per second for the (constant) nucleus orientation considered here. It is assumed that the gas drags a broad distribution of spherical dust grains, represented by 44 sets of single-size grains of mas m_i ($1 \leq i \leq 44$); the masses m_i are logarithmically equispaced, from 10^{-20} kg to 3.16×10 kg. In contrast with what was assumed in Crifo & Ro-

dionov (1997a,b), here the differential dust size distribution $g(s)$ is assumed to be a power law of the dust radius s : $g(s) \propto s^\alpha$. Following the best available fits of the Didsy experiment (Fulle et al. 1995), we adopt $\alpha = -3.5$. This power index is of course a free parameter of the model, which could be run with other α values. The nucleus and dust specific mass (also free parameters of the model) are taken to be $\rho_n = \rho_d = 10^3$ kg m $^{-3}$. The nucleus is assumed oriented with the Sun inclined at 45 degree from the nucleus axis of symmetry OY, in the XOZ symmetry plane (see Fig. 1).

The multifluid dusty gasdynamic code described in Crifo & Rodionov 1997b was re-run with the new values of R_n , f and $g(s)$ indicated above. The computed gas and dust spatial distributions are very similar to those computed in Crifo & Rodionov (1997b), except that the gas number densities are about four times greater, since the nucleus outer area is about four times smaller. The difference in f and R_n results (see Appendix D of Crifo & Rodionov, 1997a) in an increase of about 40% in the terminal dust velocities shown here on Fig. 1. This difference can be best seen on Fig. 13 of Crifo & Rodionov (1999a). The change in the shape of $g(s)$ does not affect much the dust density, except at the smallest and largest sizes, where the present densities are considerably greater than in Crifo & Rodionov (1997b). But, as we will indicate, we here study the dust impacts over a size interval which is smaller than the size interval considered in the gasdynamic code. As in Crifo & Rodionov (1997b), the spatial distribution of the dust is found to be weakly dependent upon the dust grain mass; this can be shown to be due in part to the smallness of the nucleus size: the gas-dust interaction length can be shown to be proportional to the nucleus characteristic dimension, and the longer it is, the greater will be the spatial dispersion between grains of differing mass.

As shown on Fig. 1, the presence of a concavity generates a couple of shock structures in the coma, which themselves result in the formation of two approximately hyperbolic layers of enhanced dust density (that would appear on images taken from favourable directions as “dust jets”). This enhancement of the density is due to the superposition of dust emanating from both sides of the gas shocks. Thus, to obtain a correct solution of the present problem, in the multifluid code, at any given mass, the grains emanating from the left side of the concavity, and those emanating from its right side, must be represented by separate “fluids” (see Crifo et al., 1995, Crifo & Rodionov, 1997 a – b), so there are all in all 88 dust “fluids”. Each of these dust fluids gives birth to one additional component of grains “reflected” by radiation pressure, which, strictly speaking, should also be represented by specific fluids in the gasdynamic code! However, because the perturbations of the gas by the dust are (for the present problem) very small, we ignore these “reflected” grains in the gasdynamic model. In doing so, we also ignore the perturbation of these reflected grain trajectories by the outflowing gas, an approximation which is probably acceptable outside of the gas-dust acceleration region.

The gasdynamic code provides the dust mass space density and velocity vector in the vicinity of the nucleus. We define the “terminal” dust velocities and space densities as those pre-

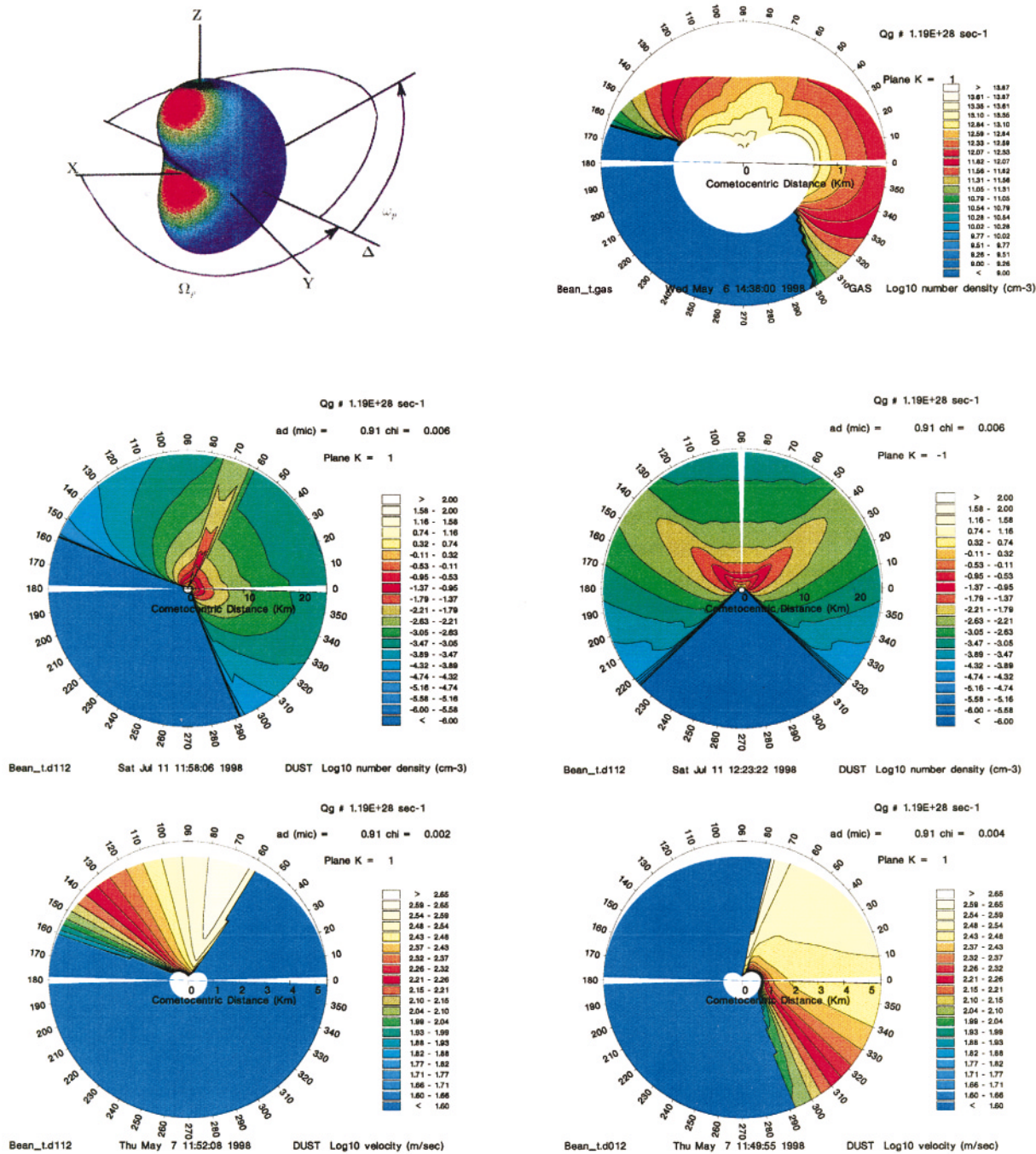


Fig. 1. Model nucleus, and resulting gas and dust distribution. The postulated nucleus is shown at *top left*, with the reference cartesian axes indicated; Δ is the nodal line of the spacecraft orbit. The Sun is inclined at 45° from OX, in the XOZ plane (angular sector 45 on the plane plots). The *upper right panel* shows the decimal logarithm of the gas number density in the XOZ plane. The *middle panels* show the decimal logarithm of the $0.91 \mu\text{m}$ radius grains number density in the planes XOZ (*left*) and XOY (*right*). The *lower panels* show the $0.91 \mu\text{m}$ radius grains velocity in the plane XOZ: (*left*) grains originating from the $Z < 0$ surface; (*right*) grains originating from the $Z > 0$ surface. Note that the two distributions overlap, to form the pseudo-jet visible on the middle left panel.

vailing over the surface where the gas drag on the grains has become negligible. This surface (about 10 km from the origin) is not a sphere, but is somewhat reminiscent from the nucleus shape. It is defined by a set of radial vectors \mathbf{r}_j ($1 \leq j \leq 3600$), in the reference system (X, Y, Z) linked to the nucleus shown

on Fig. 1. These vectors define 3600 radial directions ϕ_j , which sample a complete halfspace (which is sufficient, in view of the coma symmetry versus the XOY plane for the present orientation of the nucleus with respect to the sun). The dust “terminal” mass space density $\rho_j(s)ds$ and velocity vector $\mathbf{v}_j(s)$ are in-

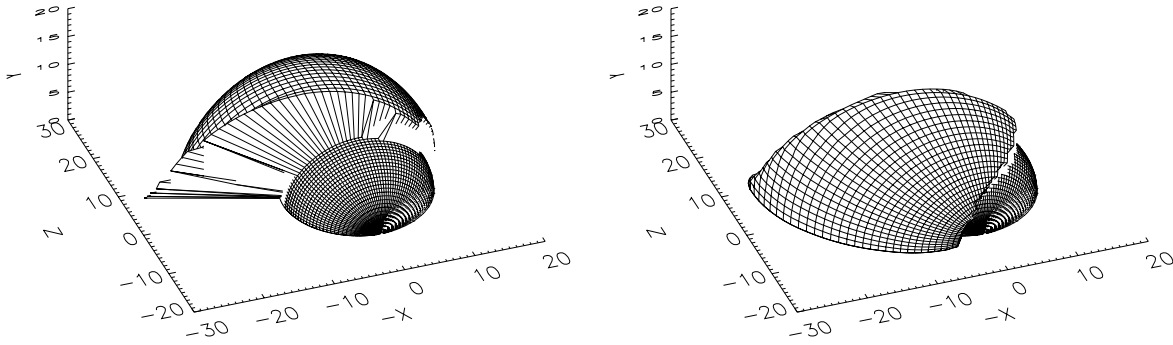


Fig. 2. 3D plot of the vector $\mathbf{r}_j + \mathbf{v}_j(s) \Delta t$, in the nucleus-attached frame XYZ, and with $\Delta t = 100$ s. The *left panels* refers to the “fluid” of dust grains originating from the $Z > 0$ half-nucleus, and the *right panel* to the dust fluid originating from the other half. Note that these two “fluids” partially overlap in the region ($X < 0, Z > 0$). The dust radius is $s = 9.8 \cdot 10^{-6}$ m. The axis scale is km. The Sun is in the XZ plane, 45° from the +X and +Z axis.

dependent from the time t , since the coma is assumed to be stationary. In general the $\mathbf{v}_j(s)$ vectors are non-radial, due e.g. to the shock structures that the grains encounter during the gas drag. Also, since the model is multifluid, for each radial direction ϕ_j , at any given dust grain mass and given position in the near-nucleus coma, several velocity and mass space density values are possible. Here, because the nucleus has one concavity only, at most two values are possible (corresponding to the mentioned two dust fluids per grain size) so that there are 7200 “terminal” velocity and density values (per grain mass) in the halfspace.

In Fig. 2 we show, for grains with $s = 9.8 \cdot 10^{-6}$ m, the vectors $\mathbf{r}_j + \mathbf{v}_j(s) \Delta t$ with $\Delta t = 100$ s, small enough that the action of the solar radiation pressure is negligible. In this way, it is possible to appreciate the expansion of a dust shell initially coincident with the “terminal” surface. The effect of the gas shock structure is apparent, resulting, in particular, in a superposition of two different dust contributions, and in a markedly non radial dust motion. In the night side (right side of the left panel of the figure) the velocity is zero, so that only the terminal surface (defined by the \mathbf{r}_j vectors) is visible. The figure also demonstrates that a single dust mass has many possible terminal velocities, simply due to the nucleus asphericity, so that it becomes impossible to define a biunivocal mass-velocity relation. This is also evident in Fig. 3, which shows an histogram of all the $v_j(s)$. For each dust mass, many velocities are possible. The crest of higher velocities is due to the shock structure, while the other lower values come from the remaining dayside coma. We believe that this histogram is specific to the assumed nucleus shape, and therefore that future simultaneous measurements of velocity histograms and of nucleus shapes should provide a sound bias for the validation of dust acceleration models.

2.2. Keplerian model and dust collection model

The aim of the dust collection model is to compute, for specific surfaces attached to a specifically oriented spacecraft on a specific orbit, the differential fluence, the cumulative fluence, the total number of grains collected and the dust flux: all these quantities will be precisely defined in the following. For this purpose, the

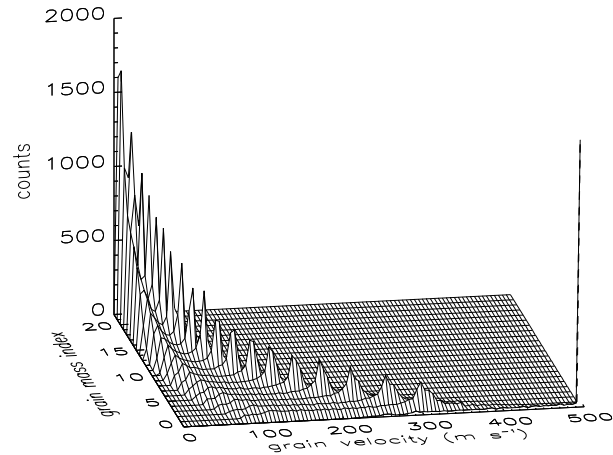


Fig. 3. Histogram of all the input $v_j(s)$ values. The 23 dust mass bins are shown, ranging from 10^{-18} kg (bin 0) to 10^{-4} kg (bin 22).

gasdynamic code is insufficient, since it provides no information on the solar radiation pressure effects, in particular on the “reflected” grain flux, nor on the solar tidal effects. For this purpose, we use a Keplerian fountain model, which computes the rigorous Keplerian heliocentric orbit connecting each terminal surface cell \mathbf{r}_j to the probe position, taking into account the solar radiation pressure and gravity acting on the dust grain. From such a rigorous orbit, the impact velocity vector $\mathbf{v}_f(s, t)$ on the probe can be computed without any approximation regarding its absolute value and orientation. The same result can be reached with classical cometocentric fountain models which take into account the tidal effects of the solar gravity on the dust motion by means of expansion series. Here, such tidal effects are automatically and rigorously taken into account by heliocentric Keplerian mechanics.

In addition to being based on gasdynamic and Keplerian mechanics, our model incorporates a probabilistic approach. On one hand, it provides a simple means of “smoothing” the results from the Gasdynamic code. Indeed, due to the poor sampling in solid angles of the gasdynamic outputs, an interpolation of these outputs is necessary. But, since in general the dust motion is not radial, it is impossible to define the neighbours of the quantity

we want to interpolate. We solve this problem by associating a sharp probability function to each quantity and to sum the contribution coming from all the cells for each given space point. On the other hand, this prepares a future extension of the model, in which statistical dispersions in grain shape and specific mass will be introduced, resulting in statistical dispersions of the dust velocity amplitude and direction at any point and for any dust mass. Thus, (1) we assume that the dust grains leave the coma cell \mathbf{r}_j with a velocity v , which is not necessarily equal to $v_j(s)$. We define a probability $p_1[v, v_j(s)]$ that a grain be ejected with velocity v , the most probable value being $v_j(s)$. Then, (2) we assume that, for each v and ϕ_j values, grains can be ejected with a direction ϕ not necessarily coincident with ϕ_j , and we define a probability $p_2[\phi, \phi_j(s)]$ that a grain be ejected in the direction ϕ , the most probable value being the $\mathbf{v}_j(s)$ direction [i.e. the direction $\phi_j(s)$]. Let us call Φ the effective solid angle of ejection of these grains (defined by p_2).

The fundamental quantity to evaluate first is the elementary number of grains which reach a collecting surface along a given direction of impact. Each dust fluid provides a different set $(v_j(s), \phi_j(s))$ at each \mathbf{r}_j , so that the following procedure applies separately to each dust fluid. From a given vector set $(\mathbf{r}_j, \mathbf{v}_j(s))$, a given time and a given probe position, only one (or no) direction ϕ will lead to grains arriving on the surface as requested. Thus, we can write for the differential number density $dN(s)$ of dust grains from the set (v, ϕ) that are crossing the elementary cell of the terminal surface and that have orbits connecting the terminal surface cell to the collecting surface (at a given time and position of the spacecraft):

$$dN(s) = \frac{\rho_j(s) p_2[\phi, \phi_j(s)]}{m(s) \Phi} p_1[v, v_j(s)] ds dv d\phi \quad (1)$$

where $d\phi$ is the elementary solid angle around the direction ϕ , $\rho_j(s)$ is the dust mass space density provided by the dust–gas interaction model and $m(s)$ is the mass of the grain of size s . The definition of the differential fluence over one probe orbit is

$$f(s)ds = \int_0^T dN(s) h(t, s) \mathbf{u}(t) \cdot [\mathbf{v}_p(t) - \mathbf{v}_f(s, t)] dt. \quad (2)$$

where T is the probe orbital period, $\mathbf{v}_p(t)$ is the probe velocity vector, $\mathbf{v}_f(s, t)$ is the impact dust velocity vector, $\mathbf{u}(t)$ is the unit vector perpendicular to the collecting surface, the symbol \cdot denotes the scalar product, and $h(t, s)$ is defined as it follows. Let us call A_0 the area of the cell j on the terminal surface. Let us consider all grains of size s ejected from this cell in a direction ϕ . At the collecting surface, these grains are spread over an area which we call $A_1(t, s)$. By definition, $h(t, s) = A_0/A_1(t, s)$. Now the problem is to compute h . For the direct component, it is clear that

$$h(s, t) = \frac{r_j^2}{(\tau(t, s)v_i(s) + r_j)^2}. \quad (3)$$

where $\tau(t, s)$ is the flight time from A_0 to A_1 , provided that the emission is “locally radial”, i.e. the 8 neighbouring vectors \mathbf{v}_j have a common intersection inside the nucleus. Fulle & Sedmak

(1988) have shown that – perhaps surprisingly – this remains true even for the reflected component (radiation pressure being dominant), provided that (i) the flight times $\tau(t, s)$ are small enough that the change in dust orbit anomaly during $\tau(t, s)$ remains smaller than $\frac{\pi}{2}$, and (ii) the emission is “locally radial”. For the present problem, the first condition is perfectly fulfilled. From Fig. 2, one can see that only a few cells near the plane XOY are deformed by local non–radial motion. Note that, in such a case both areas A_0 and A_1 are perpendicular to the starting and impact velocity vectors, respectively. Thus, the proper orientation of the areas A_0 and A_1 is taken into account in the $h(s, t)$ computation. Inserting the trivial $m(s)$ expression for spherical grains, the differential fluence per orbit, $f(s)$, is given by:

$$f(s)ds = \int_0^T \int_0^\infty \int_{4\pi} \frac{3 \rho_j(s) r_j^2 \mathbf{u}(t) \cdot [\mathbf{v}_p(t) - \mathbf{v}_f(s, t)]}{4\pi \Phi \rho_a s^3 [v\tau(t, s) + r_j]^2} \times p_1[v, v_j(s)] p_2[\phi, \phi_j(s)] dt dv d\phi ds \quad (4)$$

Only the grains characterized by

$$\mathbf{u}(t) \cdot [\mathbf{v}_p(t) - \mathbf{v}_f(s, t)] > |\mathbf{v}_p(t) - \mathbf{v}_f(s, t)| \cos \frac{w}{2} \quad (5)$$

must be considered in the integration of Eq. (4). Here, w is the full acceptance angle of the dust collecting experiment, $w = \pi$ when the fluence on a flux exposed surface has to be computed.

The probe velocity vector and its position in space are defined by the probe orbital parameters: q_p , the perinucleus distance; e_p , the probe orbit eccentricity; Ω_p , the nodal line orientation with respect to the X nucleus axis; ω_p , the perinucleus orientation with respect to the nodal line; and i_p , the probe orbit inclination with respect to the XOY nucleus symmetry plane. For each probe position in space defined by the probe radius vector $\mathbf{r}_p(t)$ (computed by means of the five mentioned parameters), the dust orbit connecting each coma cell \mathbf{r}_j and $\mathbf{r}_p(t)$ is computed taking into account its initial velocity \mathbf{v} and the solar radiation pressure force, thus obtaining the impact dust velocity vector $\mathbf{v}_f(s, t)$ and the dust flight time $\tau(t, s)$. We show in Fig. 4 an histogram of the flight times of all grains collected along a petal–like orbit of $q_p = 15 R_n$, $e_p = 9.0$, $\Omega_p = 30^\circ$, $\omega_p = 30^\circ$ and $i_p = 30^\circ$. The main crest is due to direct grains, and the other much lower crests are due to reflected grains. One sees that the times are rather small, excepted at very large masses. It means that, to allow for a nucleus rotation, it will be possible to use the present steady model at successive nucleus orientations (quasi stationary approximation).

The total number of grains collected (or total fluence), \mathcal{N} , the cumulative fluence, $h(m)$, and the dust flux $\psi(t)$ are given by:

$$\mathcal{N} = \int_{s_1}^{s_2} f(s)ds \quad (6)$$

$$h(m) = \int_{s(m)}^{s_2} f(s)ds \quad (7)$$

$$\psi(t) = \int_{s_1}^{s_2} \frac{df(s)}{dt} ds \quad (8)$$

where s_1 and s_2 are the limiting sizes considered.

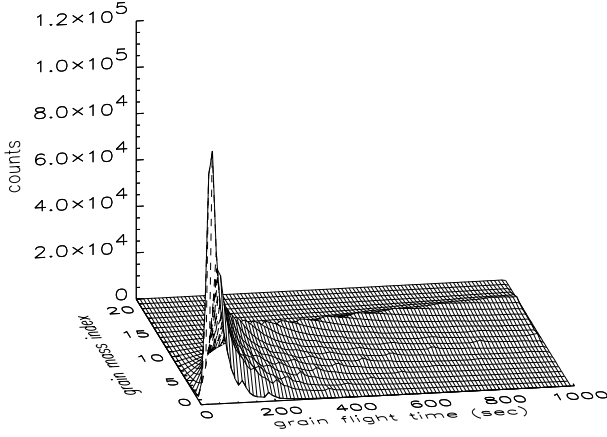


Fig. 4. Histogram of all the flight times $\tau(t, s)$ of all grains collected along a petal-like orbit of $q_p = 15 R_n$, $\Omega_p = 30^\circ$, $\omega_p = 30^\circ$, $i_p = 30^\circ$ and $e_p = 9.0$. The 23 dust mass bins are shown, ranging from 10^{-18} kg (bin 0) to 10^{-4} kg (bin 22).

As announced precedingly, we choose the restricted size range $s_1 = 9 \cdot 10^{-8}$ m and $s_2 = 3 \cdot 10^{-3}$ m. The reason for it is that, at very small sizes, a single power law distribution for $g(s)$ provides an exceedingly large impact rate (compared to what was measured on board Giotto), while, at exceedingly large sizes, the power law extrapolation is of uncertain value in the absence of any data.

In the present computations, for $p_1[v, v_j(s)]$ and $p_2[\phi, \phi_j(s)]$ we assume the following simple distributions:

$$p_1[v, v_j(s)] = \delta[v - v_j(s)] \quad (9)$$

$$\frac{p_2[\phi, \phi_j(s)]}{\Phi} = \frac{\exp - \left[\frac{1 - \frac{v \cdot v_j(s)}{v v_j(s)}}{1 - \cos \phi_0} \right]^2}{\pi^{3/2} (1 - \cos \phi_0) \operatorname{erf} \frac{2}{1 - \cos \phi_0}} \quad (10)$$

where erf is the error function and ϕ_0 is the ejection dispersion, which can be interpreted as a smoothing parameter: the lowest ϕ_0 value able to provide smooth results is chosen in all present simulations, and it does never exceed 5° .

In the following, we will also test the conjecture mentioned at the beginning of this paper, that the fluence averaged over *all* possible orbits defined by given values of q_p and e_p “is probably equal” to the fluence integrated over *one* similar orbit (with arbitrary orientation) and computed using the equivalent 1-D spherical model. In fact, the preceding statement is still imprecise: one must still define which probe surface is considered for evaluating the fluence. We here will test this conjecture for the fluence over an exposed surface ($w = \pi$) surface *permanently directed towards the nucleus*². For it, we compute the flux by means of Eqs. (4) and (8) for probe orbits covering all Euler’s

² It is evident that the conjecture is wrong for surfaces permanently oriented at a large angle to the direction of the nucleus, since in the 1-D model, the dust flows strictly radially, but not in 3-D models; on the other hand, if the total external surface of the spacecraft is used to evaluate the fluence, it is easy to show that the conjecture is trivially verified, from conservation of the dust flux.

angles i_p, ω_p, Ω_p ; then, we compute from these fluxes an average total fluence by integration over all possible Euler’s angles, with the weight $\sin i_p$. We compare the result to what we call an “isotropic total fluence” $\langle \mathcal{N}_{iso} \rangle$ which is the fluence acquired on any orbit of this shape by an uncollimated surface pointed to the nucleus, assuming a spherically symmetric dust coma with the same total dust production rate $Q(s)$; this fluence does not depend upon the value of the assumed “isotropic terminal velocity”: $\langle \mathcal{N}_{iso} \rangle = \int_0^T \psi_{iso}(t) dt$. Finally, in the following we also compare the exactly computed dust flux with what we call the “isotropic dust flux”, which is computed, for any given orbit, assuming that the collecting surface is oriented towards the nucleus center, and that there is no reflected flux as if there was no solar radiation pressure, i.e.:

$$\psi_{iso}(t) = \int_{s_1}^{s_2} \int_{4\pi} \frac{3 \rho_j(s) r_j \mathbf{r}_j \cdot \mathbf{v}_j(s)}{16 \pi^2 \rho_d s^3 r_p^2(t)} d\phi_j ds \quad (11)$$

3. Results

We have used the preceding model to compute the dust collection by a spacecraft oriented as the future “Rosetta” orbiter, i.e. one of its axis, $+z$, is maintained permanently oriented towards the nucleus, while another axis, y , parallel to that around which the solar panels can be rotated, is maintained perpendicular to the direction of the Sun. Thus, we choose for the \mathbf{u} vectors of Eq. 4, the unit vector \mathbf{k} of $+z$, the unit vector of $+y$, $\mathbf{j} = \mathbf{k} \times (-\mathbf{u}_\odot)$ (where \mathbf{u}_\odot is the unit vector directed towards the sun), and $\mathbf{i} = \mathbf{j} \times \mathbf{k}$. Since by spacecraft design y and z are perpendicular, the xyz frame is rigidly attached to the spacecraft, so that the computed dust impacts refer to well-defined spacecraft structures. The y direction is not defined when $+z$ points towards the sun: in fact in that situation, any y axis perpendicular to the z is possible. Moreover, after the passage of the spacecraft of such an eclipse point, the reference system should be rotated of 180° .

We first present results corresponding to a relatively small dust acceptance angle $w = 40^\circ$ representative of on-board dust-collecting instruments; we alternatively consider a set of circular orbits having the same large radius, and all possible orientations; then a set of circular orbits with the same small radius and all possible orientations; then elliptical orbits with the same shape and all possible orientations; finally, a set of so-called “petal-like” orbits with the same shape, but all possible orientations.

A second group of results correspond to a half space collection of dust ($w = \pi$), i.e. are suitable for a discussion of the spacecraft contamination by the dust.

3.1. Small acceptance angle: large radius circular orbits

Fig. 5 shows the total fluence, \mathcal{N} , as a function of the probe orbit Euler angles i_p and Ω_p , for a circular orbit ($e_p = 0.01$) with $q_p = 50 R_n \simeq 37.5$ km, and for a dust acceptance angle $w = 40^\circ$. This figure can be compared to Fig. 6 in F97, where w is the same, q_p is a little larger (50 km) and the sun-comet distance is 1.76 AU versus 1.06 AU here. In both cases, one sees that the antinucleus direction ($-z$ axis in Fig. 5, $-x$ axis in

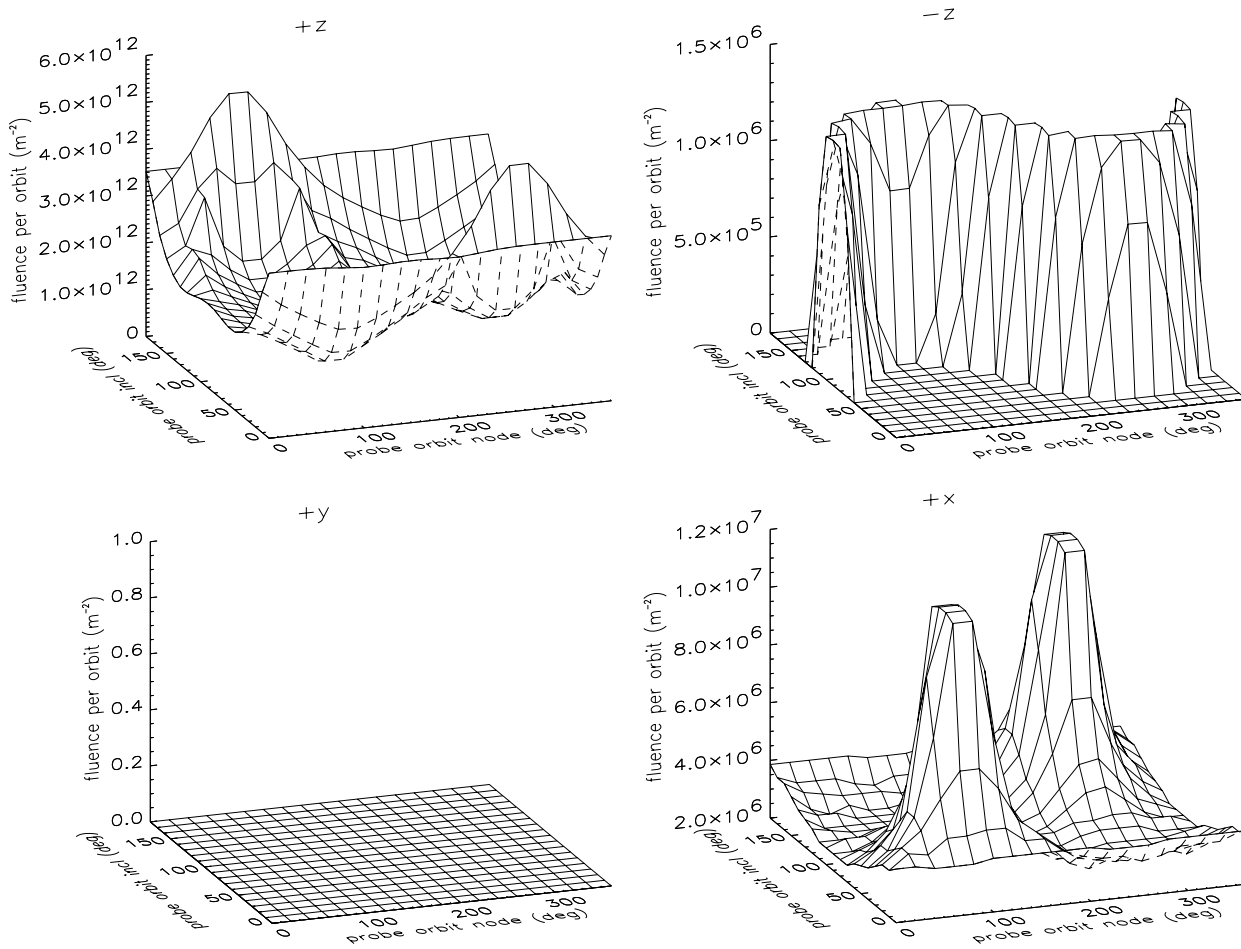


Fig. 5. Total fluence \mathcal{N} collected during a circular probe orbit with $q_p = 37$ km, sun–comet distance 1.06 AU and acceptance angle $w = 40^\circ$. The different panels refer to various pointing directions: Comet nucleus direction (+ z) and its opposite ($-z$); solar panel axis (+ y); direction perpendicular to the y and z axes (+ x). The average fluence collected from the nucleus direction is $1.67 \cdot 10^{12} \text{ m}^{-2}$, close to the isotropic total fluence ($1.66 \cdot 10^{12} \text{ m}^{-2}$).

F97) can collect reflected dust only for orbits placing the probe between the sun and the comet nucleus. Since in F97 the orbit angles are defined with respect to the sun, this happens in F97 for $i_p = 0, \pi$ and $\Omega_p = 0, \pi, 2\pi$. On the contrary, in Fig. 5 the probe orbit angles are linked to the nucleus, so that the orbits placing the probe between the sun and the nucleus are defined by the angles where the fluence has the maximum on the $-z$ direction (a sinusoidal crest).

In F97, since the dust ejection is strongly peaked towards the sun, the fluence coming from the nucleus also has its largest values when the probe is between the sun and the comet nucleus, i.e. the two 3D fluence plot relative to the $\pm x$ axes (of F97) are identical. This happens also in Fig. 5. In fact, a sinusoidal crest similar to that relative to the $-z$ axis is visible in $+z$, although it is masked by the fact that there is a significant fluence for the other probe orbit angles. This, in turn, is due to the present much lower dust ejection anisotropy, compared to the dust environment assumed in F97, and to the fact that the gas shock, which provides the absolute maxima of the fluence relative to the nucleus direction (+ z axis), is not exactly pointing towards

the sun. The fact that here we are dealing with a less anisotropic coma is confirmed by the lower ratio between the fluences relative to the $\pm z$ axes (about $3 \cdot 10^{-7}$ in Fig. 5) with respect to F97 (about 10^{-4} between the $\pm x$ axes in Fig. 6 of F97). We recall that this ratio has a minimum for isotropic comae. In Fig. 5, since the adopted dust environment is time independent, all the probe orbits with $i_p = 0, \pi$ and any Ω_p must provide the same fluence along all the probe axes. On the contrary, since in F97 the dust loss rate is time-dependent, different Ω_p values imply a different probe position at the starting sun–comet distance, so that the fluence for these angles changes according to the comet activity dependence upon heliocentric distance.

In F97, the $\pm y$ axes are linked to the probe velocity vector, so that they can collect dust when this vector points to the sun. On the contrary, here the $\pm y$ axes are always perpendicular both to the nucleus and to the sun directions, so that, for a small acceptance angle w , the fluence along these directions must be zero. This is confirmed by the result in Fig. 5. For some probe orbit orientations, the $+x$ axis points always towards the sun, in particular when the probe orbit spin points towards the solar

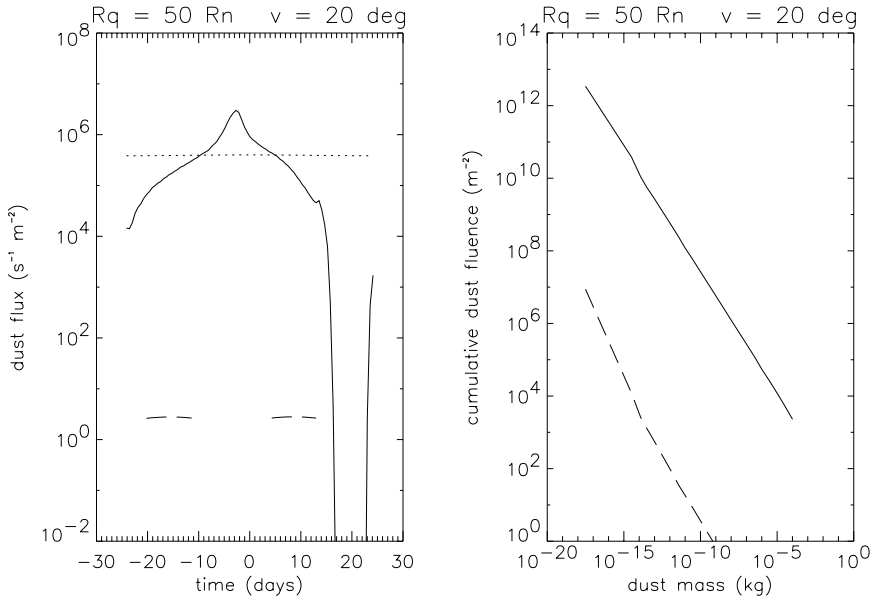


Fig. 6. Flux $\psi(t)$ (left panel) and cumulative fluence $h(m)$ (right panel) collected during a circular probe orbit with $q_p = 37$ km, $e_p = 0.01$, $\omega_p = 30^\circ$, $\Omega_p = 30^\circ$, $i_p = 30^\circ$, sun–comet distance 1.06 AU and acceptance angle $w = 40^\circ$. The different panels refer to various pointing directions: Comet nucleus direction ($+z$, continuous line); direction perpendicular to the y and z axes ($+x$, dashed line); isotropic flux (constant dotted line).

or antisolar direction. Fig. 5 shows that this happens for $i_p = \frac{\pi}{4}$ and $\Omega_p = \frac{\pi}{2}$ (and the symmetric case). For these orbits, the $+x$ axis in Fig. 5 corresponds exactly to the $\pm z$ axis in F97, and the related fluence provides the largest possible collection of purely reflected grains. The comparison confirms that here the ratio between reflected and direct grains which can be collected is lower ($5 \cdot 10^{-6}$ in Fig. 5) than in F97 (10^{-3} in F97, Fig. 6). Taking into account the different reference systems of the orbit angles in the two figures, the shape of the maxima for the reflected grains is very similar in the two cases. The main difference between the two plots is that in Fig. 5 the $+x$ axis collects dust for every probe orbit orientation, whereas in F97 the fluence relative to the corresponding $-z$ axis is exactly zero outside of the favourable orbits because the $\pm y$ axes are always perpendicular to the sun direction, so that for every probe orbit orientation there is at least one position on the probe orbit where the $+x$ axis points towards the sun.

Figs. 6 and 7 show fluxes and cumulative fluences for three orbits of the set shown in Fig. 5. Fig. 6 shows the flux and the cumulative fluence for an orbit with arbitrary orientation. The probe crossing of the coma shock structure is well visible in the flux on the $+z$ direction, as well as the strong night-side dip. This flux can be directly compared to the “isotropic flux” defined precedingly: although the latter is the average of the $+z$ flux, the enormous time dependence of the $+z$ flux is apparent.

The cumulative fluence on the $+z$ direction coincides with the “isotropic fluence”, because it is dominated by the dust in the dayside coma (direct grains only). For this orbit, the only other direction able to collect reflected grains is the $+x$ one, when it points towards the sun. The corresponding cumulative fluence is clearly different from the $+z$ one, due to selective effects of the solar radiation pressure on the grain sizes.

Fig. 7 (top) shows the flux and the cumulative fluence for a probe orbit located in the comet terminator. In this case no night dip is possible, and the probe crosses the coma shock

twice. As it must be, the flux of reflected grains on the $+x$ direction is constant. This figure can be compared with Fig. 4 in F97: the flux of relected grains is very similar, although in F97 it increases with time due to the heliocentric dependence of the comet activity. The main difference is that here, due to the much lower coma anisotropy, the direct flux always largely dominates the reflected one.

Fig. 7 (bottom) shows a probe orbit with the nodal line aligned to the sun–comet direction, thus allowing solar eclipses and exact passages between the sun and the comet. Since the coma shock does not point towards the sun, in this case the probe does not cross the shock. When the probe is on the dayside coma, the flux on the $+z$ direction is relatively constant. On the nightside coma, a strong night side dip is visible, but during the solar eclipse the $+z$ direction collects reflected grains. It is obvious that this is possible only because in our model we completely neglect possible interactions between reflected grains and the gas in the coma, which can well completely prevent any dust detection in this peculiar case (solar eclipse will be avoided by the Rosetta spacecraft). These are also collected by the $+x$ and $-z$ directions, when these directions point towards the sun: since the probe orbit is circular, all the reflected fluxes are identical. As in Figs. 6 and 7 (top), the direct cumulative fluence is significantly different from the reflected ones. This figure can be compared with Fig. 3 in F97. Regarding the flux on the nucleus direction, similar strong day/night effects are observed, although here the reflected flux is lower than in F97. Moreover, the reflected fluxes does not depend on time here, due to the stationary coma we assume. Finally, comparing the cumulative fluences in Figs. 6 and 7, we can conclude that their absolute values do not depend upon the specific probe orbit orientation.

3.2. Small acceptance angle: small radius circular orbits

Fig. 8 shows the total fluence per orbit for the same parameters as in Fig. 5, except that the probe–nucleus distance is now taken

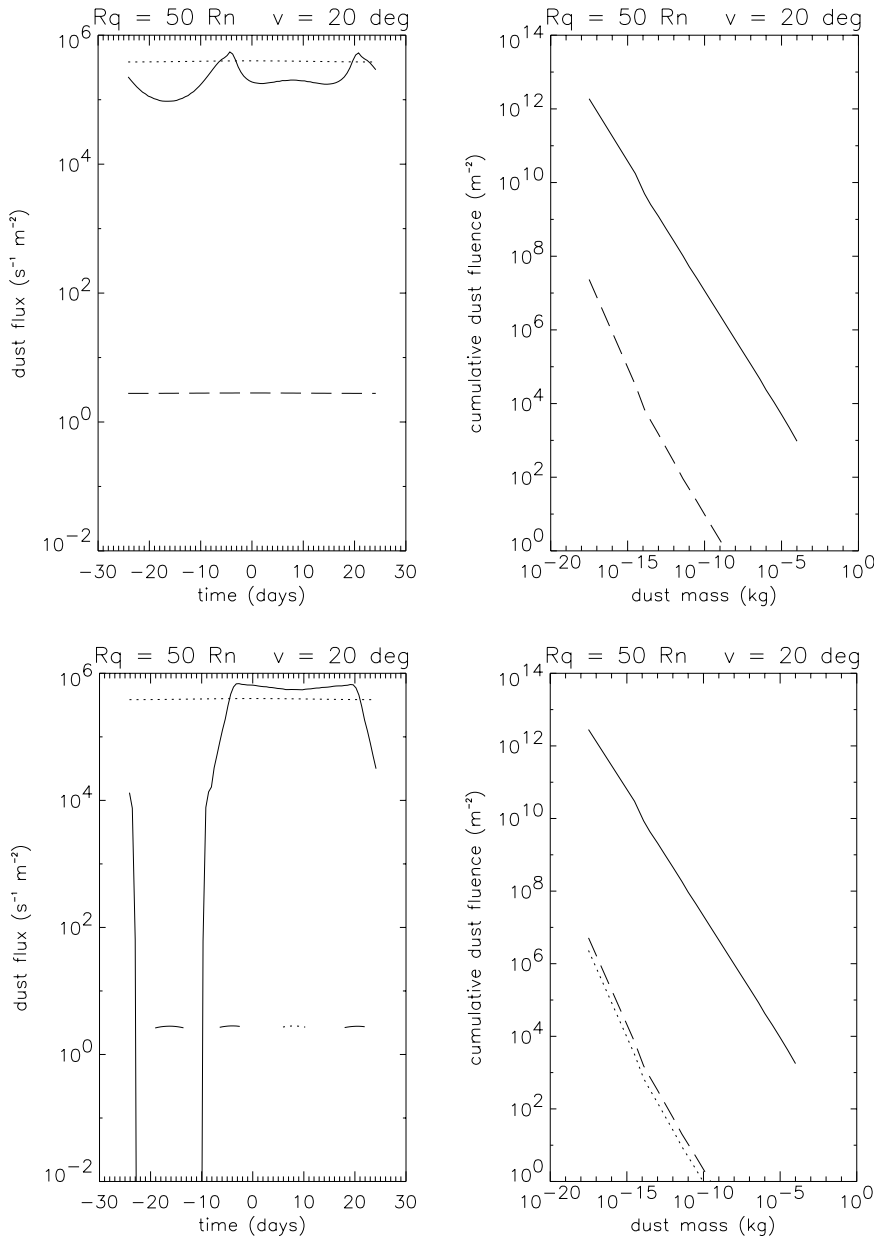


Fig. 7. Flux $\psi(t)$ (left panel) and cumulative fluence $h(m)$ (right panel) collected during a circular probe orbit with $q_p = 37$ km, $e_p = 0.01$, $\omega_p = 30^\circ$, $\Omega_p = 90^\circ$, $i_p = 45^\circ$ (top panels), $i_p = 135^\circ$ (bottom panels), sun–comet distance 1.06 AU and acceptance angle $w = 40^\circ$. The different lines refer to various pointing directions: Comet nucleus direction (+z, continuous line); direction perpendicular to the y and z axes (+x, dashed line); isotropic flux (constant dotted line).

to be $q_p = 20 R_n \simeq 15$ km. Since the probe orbital period increases as $q_p^{1.5}$, while the dust space density decreases as q_p^{-2} , we must expect an increase of a factor $q_p^{-0.5}$ of the collected fluences. This is exactly what happens. Moreover, no difference is visible between the plots of Fig. 8 and those of Fig. 5, when the preceding scaling is taken into account. This same scaling also applies to the isotropic total fluence: when we average the fluences relative to the +z axis in Figs. 5 and 8, taking into account the weight $\sin i_p$, we obtain $1.67 \cdot 10^{12} \text{ m}^{-2}$ for $q_p = 50 R_n$ and $2.66 \cdot 10^{12} \text{ m}^{-2}$ for $q_p = 20 R_n$, in perfect agreement with the isotropic values. The same comparison of the total fluences collected for different q_p values is provided by Figs. 2 and 6 in F97: surprisingly, the highest fluences are obtained there for the highest q_p . This apparent paradox is explained by the time–dependent dust loss rate assumed in F97: the loss rate

decreases there as the 6th power of the sun–comet distance, so that, when q_p is larger, the probe samples a comet approaching the sun and becoming more and more active, so that the probe has time to collect more dust than during a much shorter orbit close to the nucleus.

Fig. 9 shows the flux and cumulative fluence for one of the probe orbits of Fig. 8. In order to distinguish the effects due to the change in probe–nucleus distance, comparison must be made with Fig. 6. In general, the fluxes are higher, due to the lower probe–nucleus distance. The differences among the fluences are smaller, due to the much longer probe orbital period in Fig. 6 (one month) than in Fig. 9 (two weeks). Moreover, since the probe crosses the coma shock closer to the nucleus, its signature appears sharper. It is clear that the probe–nucleus distance introduces much smaller variations in the results than the coma

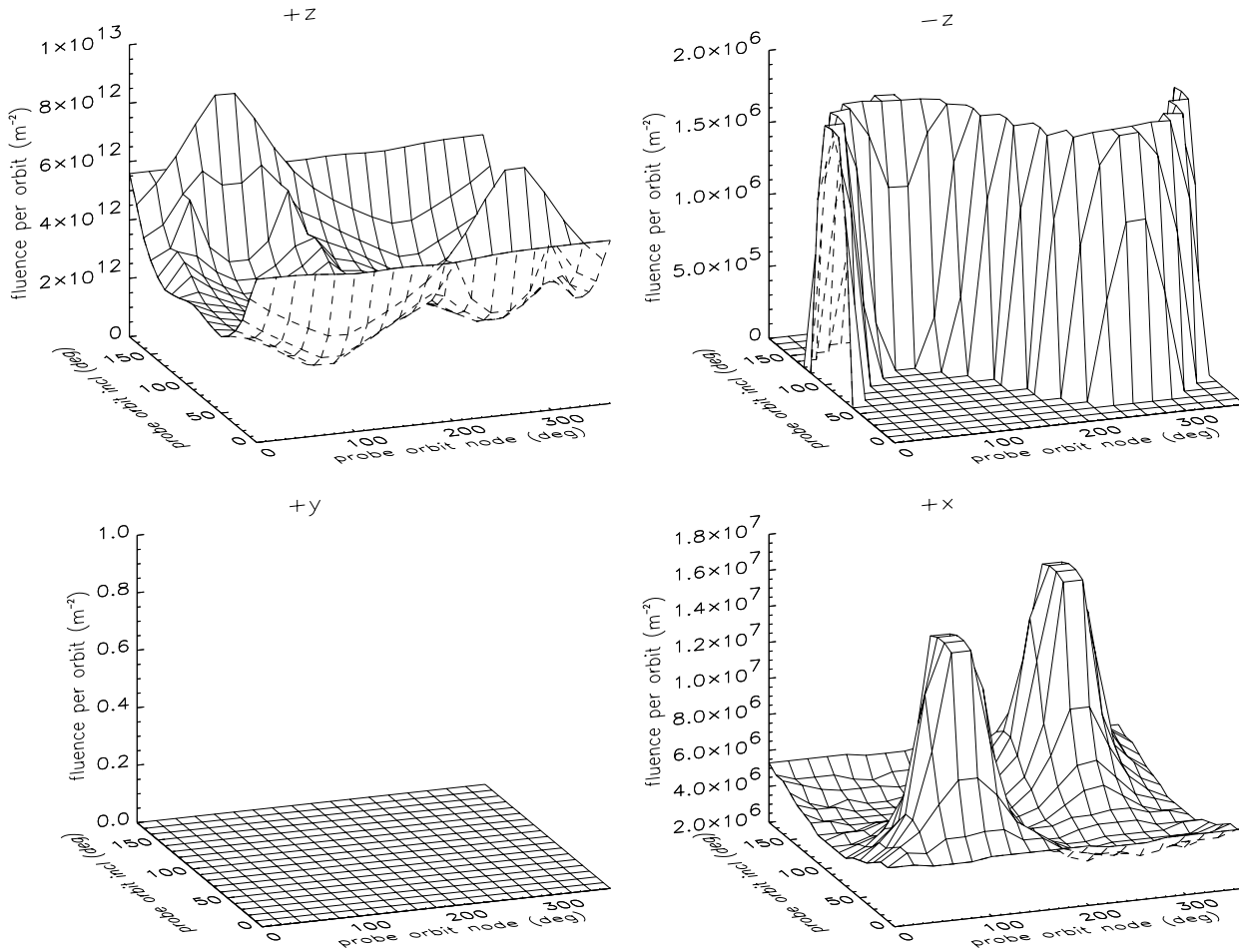


Fig. 8. Total fluence \mathcal{N} collected during a circular probe orbit with $q_p = 15$ km, sun-comet distance 1.06 AU and acceptance angle $w = 40^\circ$. The different panels refer to various pointing directions: Comet nucleus direction (+z) and its opposite (-z); solar panel axis (+y); direction perpendicular to the y and z axes (+x). The average fluence collected from the nucleus direction is $2.66 \cdot 10^{12} \text{ m}^{-2}$, close to the isotropic total fluence ($2.62 \cdot 10^{12} \text{ m}^{-2}$).

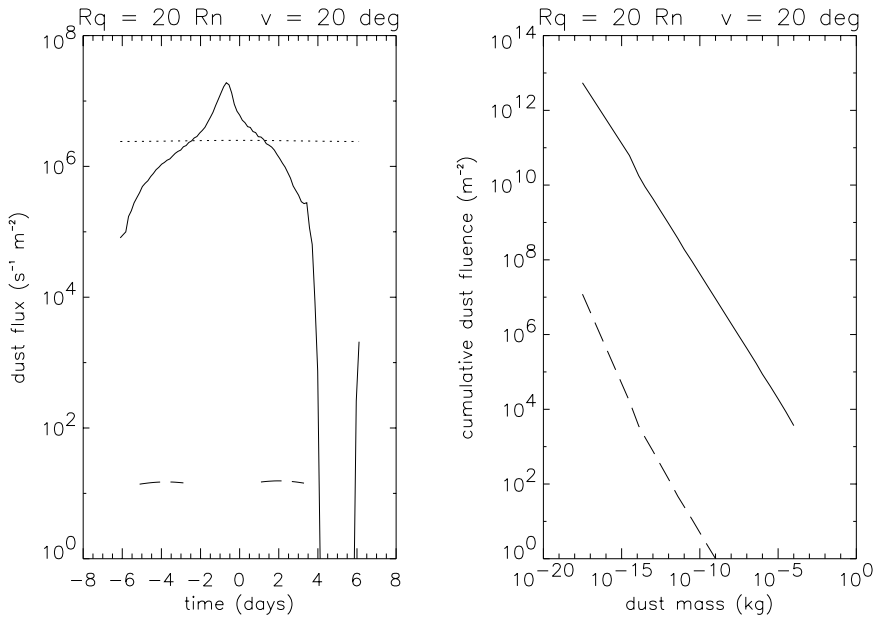


Fig. 9. Flux $\psi(t)$ (left panel) and cumulative fluence $h(m)$ (right panel) collected during a circular probe orbit for $q_p = 15$ km, $e_p = 0.01$, $\omega_p = 30^\circ$, $\Omega_p = 30^\circ$, $i_p = 30^\circ$, sun-comet distance 1.06 AU and acceptance angle $w = 40^\circ$. The different lines refer to various pointing directions: Comet nucleus direction (+z, continuous line); direction perpendicular to the y and z axes (+x, dashed line); isotropic flux (constant dotted line).

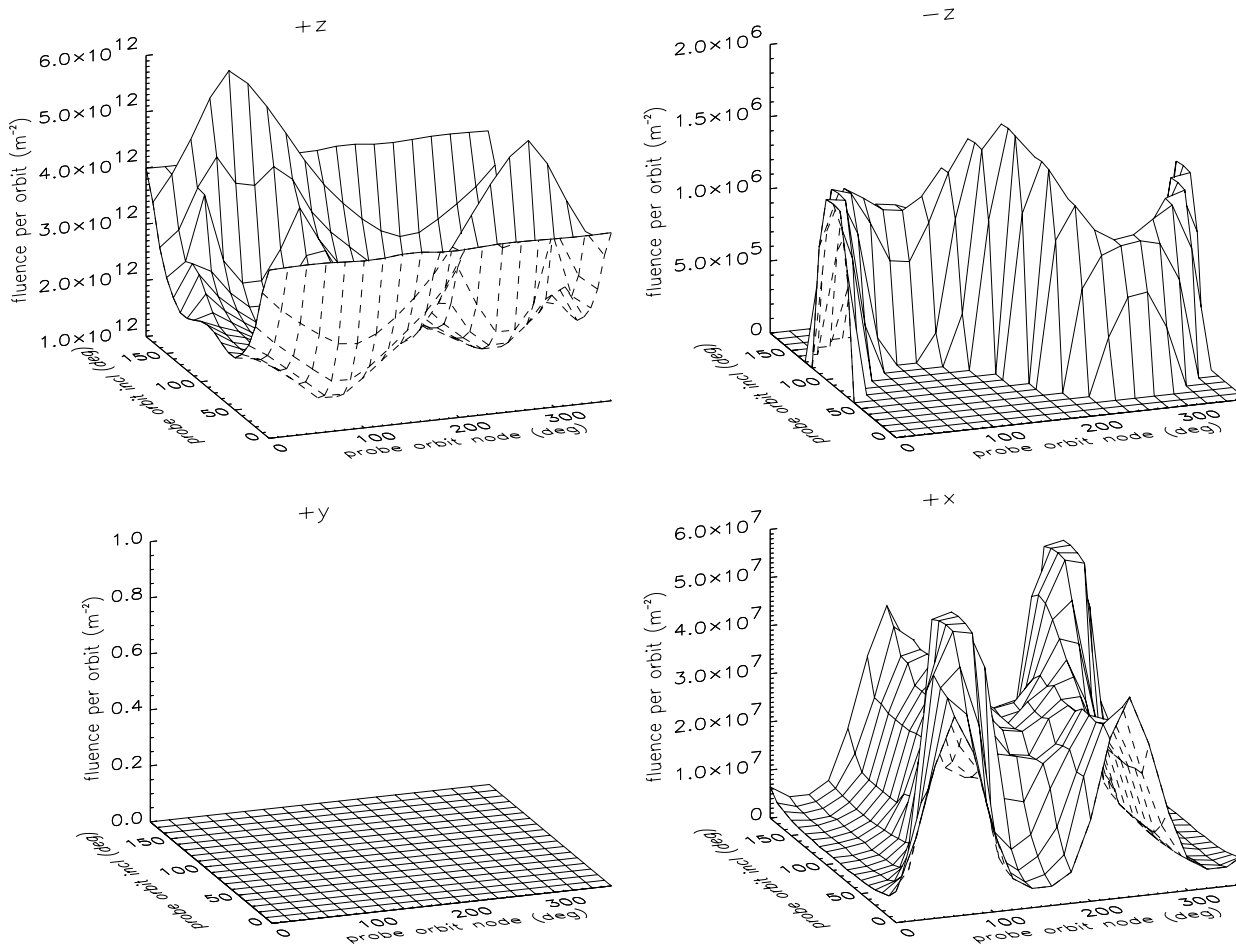


Fig. 10. Total fluence \mathcal{N} collected during an elliptical probe orbit with $q_p = 15$ km, $e_p = 0.9$, $\omega_p = 30^\circ$, sun–comet distance 1.06 AU and acceptance angle $w = 40^\circ$. The different panels refer to various pointing directions: Comet nucleus direction (+ z) and its opposite (– z); solar panel axis (+ y); direction perpendicular to the y and z axes (+ x). The average fluence collected from the nucleus direction is $1.95 \cdot 10^{12} \text{ m}^{-2}$, close to the isotropic total fluence ($1.91 \cdot 10^{12} \text{ m}^{-2}$).

anisotropy, entirely confirming on this the conclusions reached in F97. For this reason, we do not show fluxes and fluences for other probe orbit parameters: they can be obtained from Fig. 7 by applying the proper probe–nucleus distance scaling.

3.3. Small acceptance angle: elliptical orbits

Fig. 10 shows the total fluence per orbit for an elliptical orbit with $q_p = 20 R_n$, $e_p = 0.9$, $\omega_p = 30^\circ$ and $w = 40^\circ$.

Since the probe–nucleus distance changes by a factor 20, we would expect fluence changes much greater than in Figs. 5 and 8. However, although the received dust flux is much lower far from the nucleus than close to it, the time the probe spends far from the nucleus is much longer: these opposite effects almost mutually compensate. In fact, the flux from the nucleus direction (+ z axis) is very similar to that in Figs. 5, 8 and 10. Differences are more apparent in the flux of reflected grains: in the antinucleus direction (– z), the changes of the peak values are due to the differing orientation of the elliptical orbit: the – z axis points towards the sun when the probe is closest to the sun

for the node values providing the largest fluence. Since now the orbit is not a circle, orbits characterized by zero inclination and different node values are not identical. This explains the large fluence variations on the + x axis for these probe orbit parameters: the largest fluences are obtained for those orbit orientations putting the + x axis towards the sun when the probe is closest to the nucleus. When we neglect these effects, due to the elliptical orbit shape, the two main fluence maxima are similar to those in Figs. 5 and 8. Regarding the absolute fluence values, we see that the fluences on the + z axis are similar to those in Fig. 5: this is due to the fact that the much longer orbital period of the probe, 320 days versus 12, compensates the much higher average probe–nucleus distance. On the contrary, the fluence on the + x axis is up to five times higher than in Fig. 5 (and four times than in Fig. 8): this shows that the ratio between the direct and reflected fluences depends on the probe orbit eccentricity. Finally, the isotropic total fluence ($1.91 \cdot 10^{12} \text{ m}^{-2}$) is found very close to the averaged fluence on the + z axis ($1.94 \cdot 10^{12} \text{ m}^{-2}$).

Fig. 11 shows the flux and cumulative fluence for individual probe orbits with the same parameters as in Fig. 10. Fig. 11 (top)

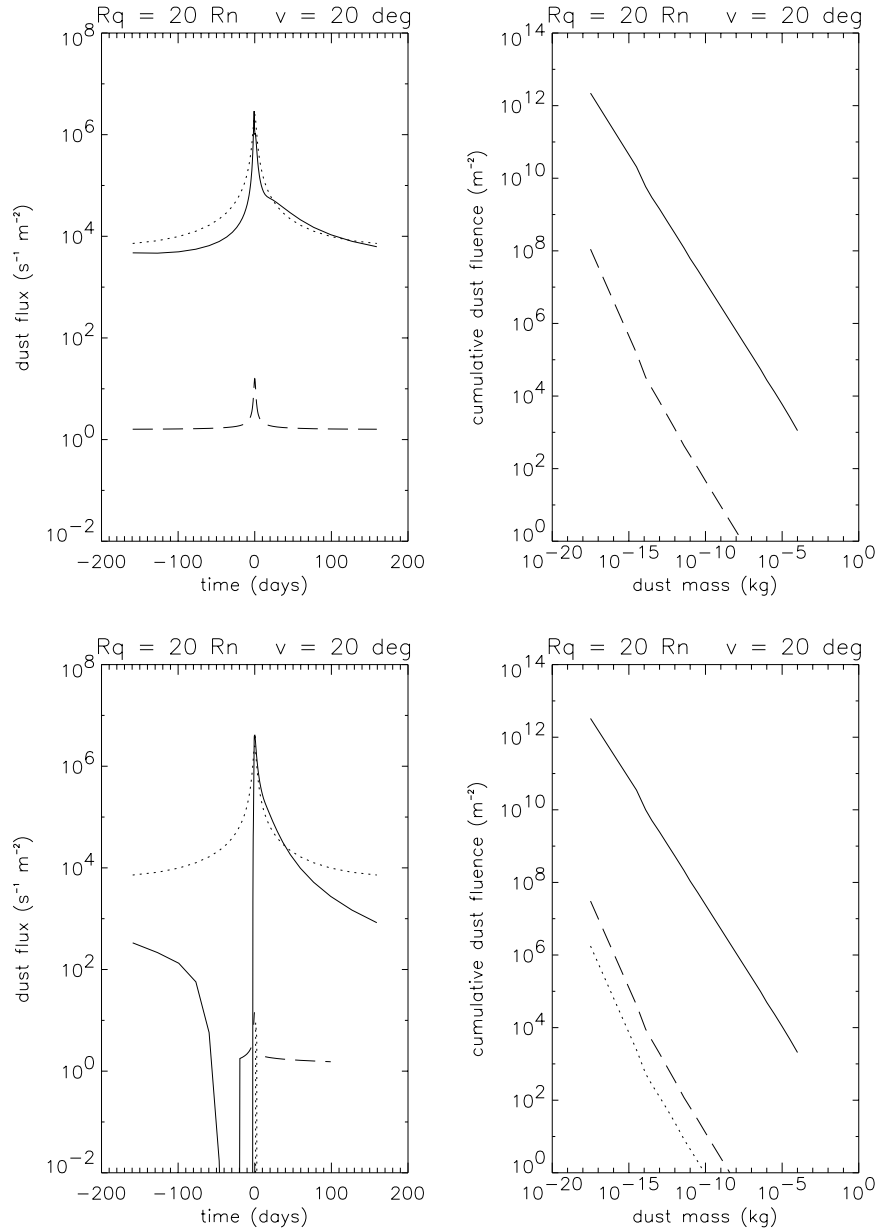


Fig. 11. Flux $\psi(t)$ (left panel) and cumulative fluence $h(m)$ (right panel) collected during a probe orbit with $q_p = 15$ km, $e_p = 0.9$, $\omega_p = 30^\circ$, $\Omega_p = 90^\circ$, $i_p = 45^\circ$ (top panels), $i_p = 135^\circ$ (bottom panels), sun–comet distance 1.06 AU and acceptance angle $w = 40^\circ$. The different lines refer to various pointing directions: Comet nucleus direction (+z, continuous line); direction perpendicular to the y and z axes (+x, dashed line); isotropic flux (dotted line).

refers to a probe orbit inside the comet terminator. In this case, the isotropic flux well approximates the flux on the +z direction. Since most of the time is spent by the probe very far from the nucleus, the shock crossings are not visible. The flux of reflected grains on the +x direction is interestingly almost constant far from the nucleus, differing on this from the direct one. Fig. 11 (bottom) considers a probe orbit with its nodal line aligned to the sun–comet direction. In this case, the isotropic flux provides a completely meaningless prediction. This further confirms that the coma anisotropy, coupled to the probe orbit orientation, is by far the comet feature exerting the strongest influence on the results. In Fig. 11 (bottom), a very strong night dip is observed. Moreover, since the +z direction points to the sun when the probe is very far from the sun, no reflected dust is collected in the nucleus direction, in contrast with what happens in Fig. 12. The

cumulative fluences of direct and reflected grains, respectively, show shapes very similar to those in Figs. 6, 7, and 9. However, the ratios among the absolute values change. In particular, in Fig. 11 the ratio of the cumulative fluence on the +x direction reaches its highest values, due to the slower decrease of the corresponding reflected flux far from the nucleus with respect to the direct grains one.

3.4. Small acceptance angle: petal-like orbits

Due to their very long orbital period, it is improbable that elliptical orbits will be adopted in order to sample different coma distances. Petal-like orbits offer an useful alternative for such a purpose. They simply consists of two hyperbolic arches: when the probe reaches the largest nucleus distance, at 90° from the

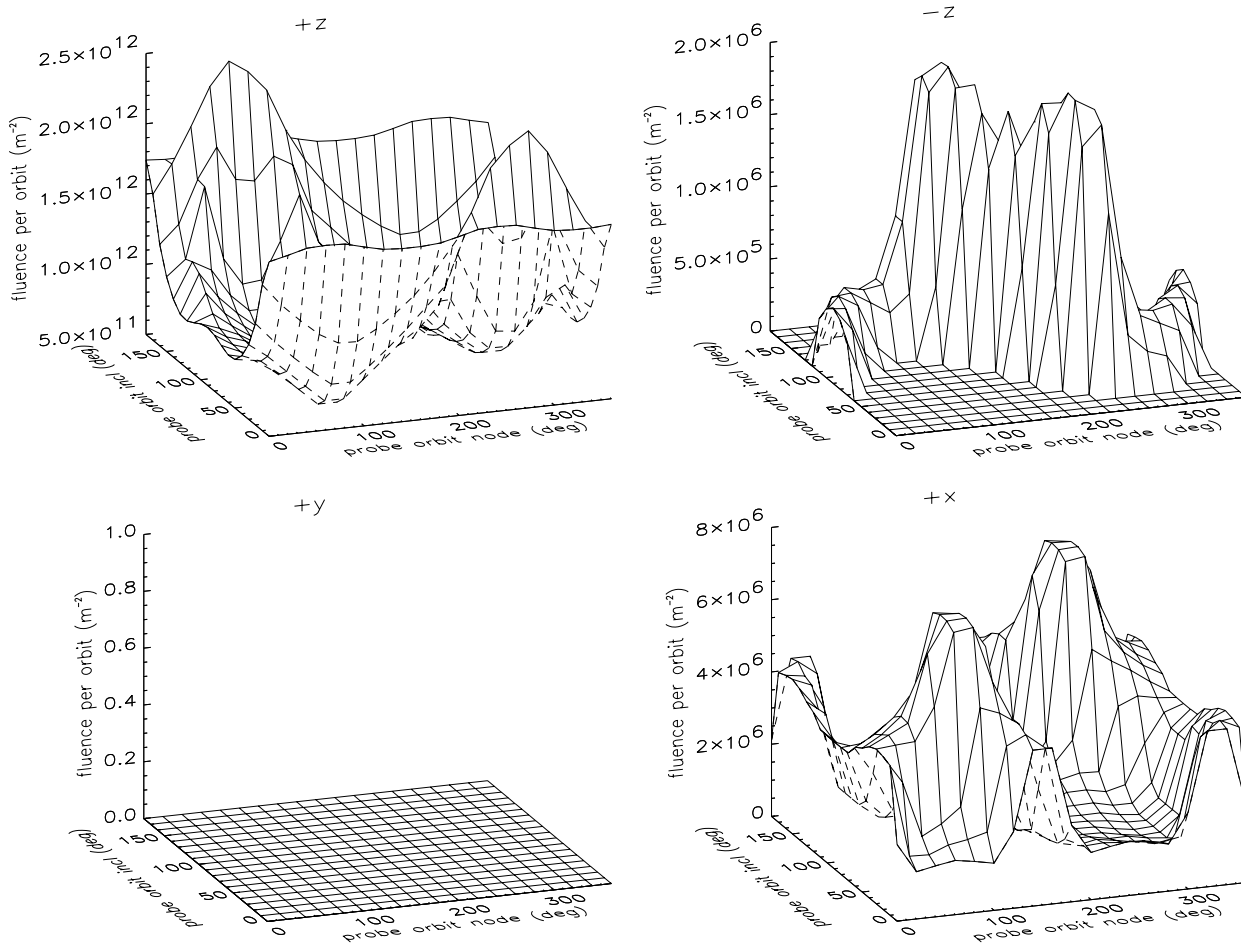


Fig. 12. Total fluence \mathcal{N} collected during a petal-like probe orbit with $q_p = 15$ km, $e_p = 9.0$, $\omega_p = 30^\circ$, sun-comet distance 1.06 AU and acceptance angle $w = 40^\circ$. The different panels refer to various pointing directions: Comet nucleus direction ($+z$) and its opposite ($-z$); solar panel axis ($+y$); direction perpendicular to the y and z axes ($+x$). The average fluence collected from the nucleus direction is $8.51 \cdot 10^{11} \text{ m}^{-2}$, close to the isotropic total fluence ($8.48 \cdot 10^{12} \text{ m}^{-2}$).

perinucleus, thrusters are activated to inject the probe in the corresponding symmetrical hyperbolic arch. Thus one obtains a much shorter orbital period, but the price to pay is a high fuel consumption.

Fig. 12 shows the total fluences for the following petal-like orbits: $q_p = 20 R_n$, $e_p = 9.0$, $\omega_p = 30^\circ$ and $w = 40^\circ$. Due to their shape, petal-like orbits have two perinucleus passes for each orbit. However, the plots in Fig. 12 do not reveal it, since at least one of these passes lies in the nightside coma. Thus, all the plots are very similar to those in Fig. 10. The lower absolute values are simply due to the much shorter orbital period, 25 days versus 320. The adopted orbits introduces probe-nucleus distance variations of a factor 10, similar to the adopted elliptical orbit. For the same reason, the ratio between the direct and reflected fluences is similar to the elliptical case, i.e., is in both cases higher than for circular orbits. Here also, we find that the isotropic total fluence ($8.48 \cdot 10^{11} \text{ m}^{-2}$) is very close to the averaged fluence on the $+z$ axis ($8.51 \cdot 10^{11} \text{ m}^{-2}$).

Fig. 13 presents the flux and cumulative fluence for one arbitrarily selected petal-like probe orbit. The latter simply reflects

the double perinucleus passage of each petal-like orbit, while the former is more complex, due both to the shock crossing (the highest flux peak) and to the nightside coma pass (dip). For the particular probe orbit orientation adopted here, the $+x$ axis points to the sun for most of the time spent far from the nucleus. The ratio of the reflected fluence to the direct one is the same observed in all previous fluence plots.

Fig. 14 considers the same petal-like orbit, but located at the comet terminator: in this case, the isotropic flux is in good agreement with the real one. As usually, this orbit orientation provides the highest value of the reflected flux and fluence. Fig. 15 shows that, changing the probe orbit orientation, the differences between the isotropic flux and the real one can become enormous. For an orbit with the nodal line aligned to the sun-comet direction, which does not cross the coma shock, the dayside orbit provides similar isotropic and real dust fluxes. On the contrary, on the nightside, the isotropic flux is totally in error. As usually, this orbit allows the $-z$ axis to collect reflected grains, when the probe is between the sun and the nucleus.

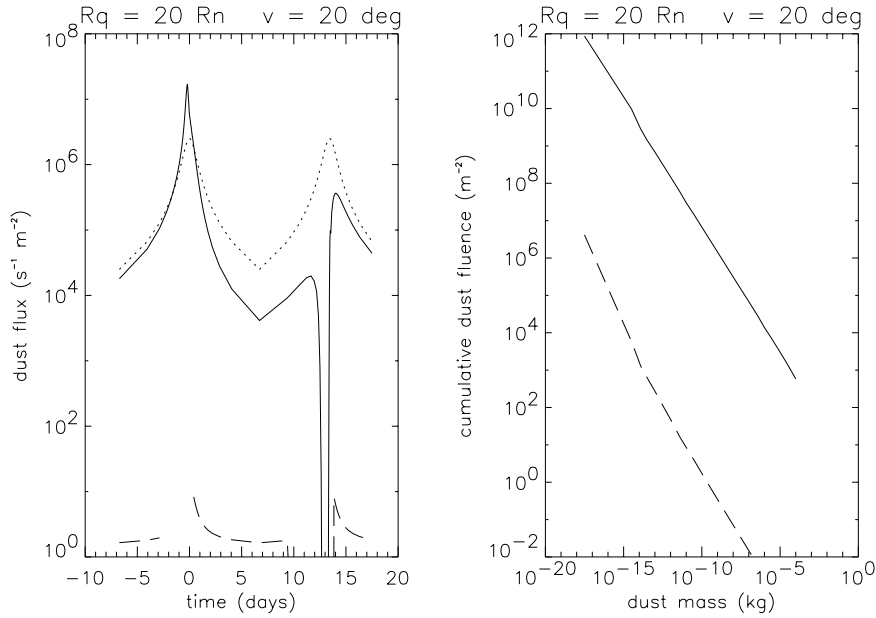


Fig. 13. Flux $\psi(t)$ (left panel) and cumulative fluence $h(m)$ (right panel) collected during a petal-like probe orbit with $q_p = 15$ km, $e_p = 9.0$, $\omega_p = 30^\circ$, $\Omega_p = 30^\circ$, $i_p = 30^\circ$, sun-comet distance 1.06 AU and acceptance angle $w = 40^\circ$. The different lines refer to various pointing directions: Comet nucleus direction ($+z$, continuous line); direction perpendicular to the y and z axes ($+x$, dashed line); isotropic flux (upper dotted line).

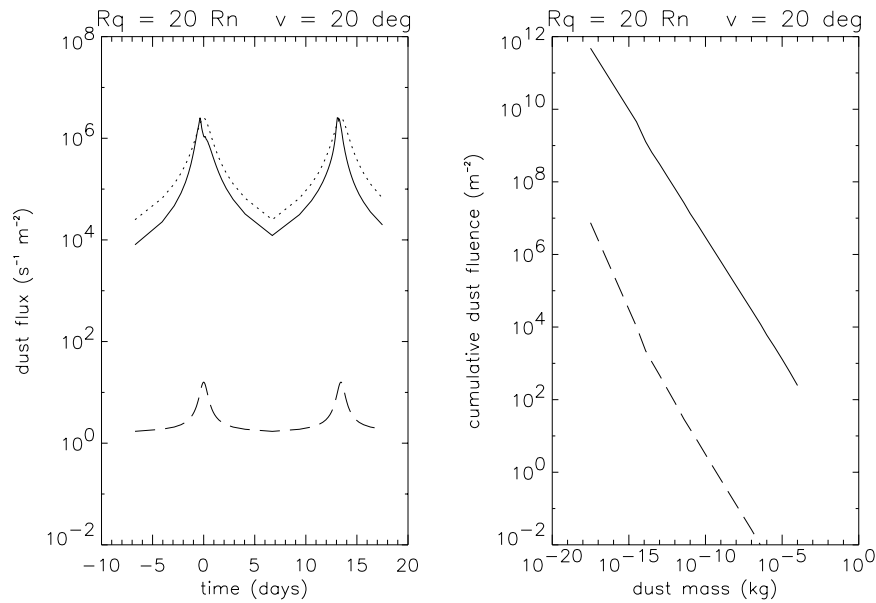


Fig. 14. Flux $\psi(t)$ (left panel) and cumulative fluence $h(m)$ (right panel) collected during a petal-like probe orbit with $q_p = 15$ km, $e_p = 9.0$, $\omega_p = 30^\circ$, $\Omega_p = 90^\circ$, $i_p = 45^\circ$, sun-comet distance 1.06 AU and acceptance angle $w = 40^\circ$. The different lines refer to various pointing directions: Comet nucleus direction ($+z$, continuous line); direction perpendicular to the y and z axes ($+x$, dashed line); isotropic flux (upper dotted line).

3.5. Hemispherical acceptance, circular orbits with a large radius

In Fig. 16 we return to the probe orbit parameters of Fig. 5, but now the dust acceptance angle is set to $w = 180^\circ$. In other words, Fig. 16 shows the dust total fluence on exposed probe surfaces.

As expected, the fluence on the $+z$ axis is the same as in Fig. 5, since direct grains largely dominate on the reflected ones. The results are different for the antinucleus direction ($-z$), because now the large acceptance angle allows to collect dust for all probe orientations, except those keeping the direction of the sun inside this surface during the whole probe orbit. Since these orbits are exactly those putting the $+x$ axis towards the sun during the whole probe orbit, these minima are obtained exactly for the probe orbit angles providing the largest fluences along the

$+x$ axis in Fig. 5. This is the conclusions arrived at in F97. The other surfaces are now also able to collect direct grains, thanks to the large acceptance angle, so that the fluences along the $+y$ and $+x$ axes are very similar to that along $+z$. The absolute values are however lower, since these surfaces collect only non radially moving direct grains, and since the collection efficiency is further reduced by the flux scalar product in Eq. 1. Still, the non radiality of the direct dust flux allows these surface to collect about the 0.5% of the direct dust flux collected on the nucleus direction: this is thousands times more than the reflected dust flux! This demonstrates that the proper allowance for non radial dust motion is fundamental for the design of an orbital strategy which can eliminate or minimize the contamination of critical surfaces (e.g. radiators).

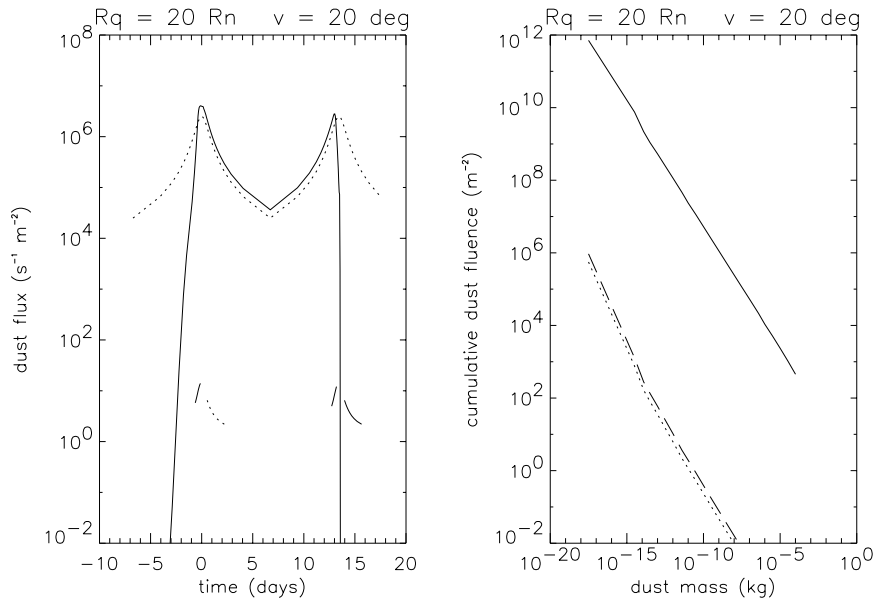


Fig. 15. Flux $\psi(t)$ (left panel) and cumulative fluence $h(m)$ (right panel) collected during a petal-like probe orbit with $q_p = 15$ km, $e_p = 9.0$, $\omega_p = 30^\circ$, $\Omega_p = 90^\circ$, $i_p = 135^\circ$, sun-comet distance 1.06 AU and acceptance angle $w = 40^\circ$. The different lines refer to various pointing directions: Comet nucleus direction (+z, continuous line) and its opposite (-z, lower dotted line); direction perpendicular to the y and z axes (+x, dashed line); isotropic flux (upper dotted line).

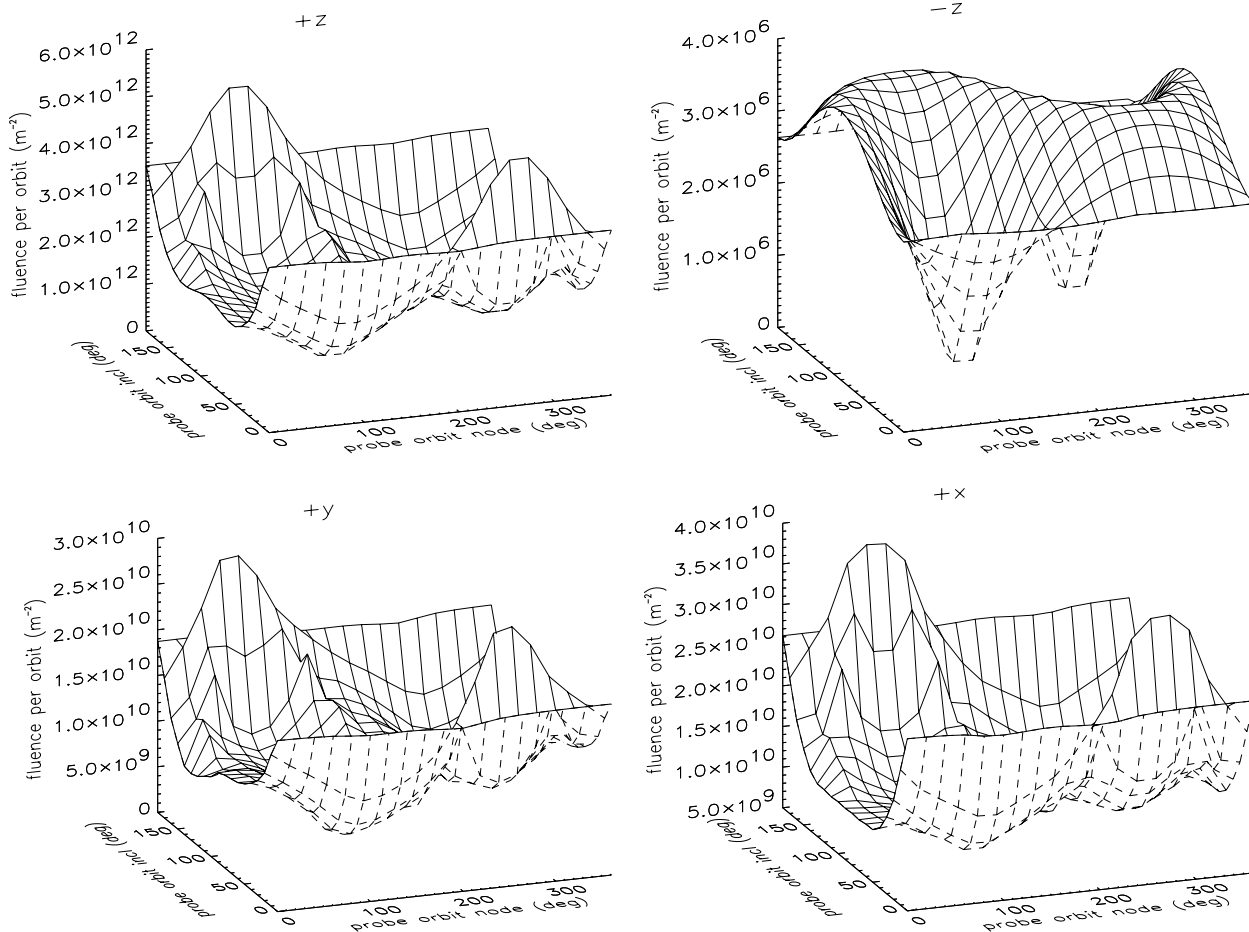


Fig. 16. Total fluence \mathcal{N} collected during a circular probe orbit with $q_p = 37$ km, sun-comet distance 1.06 AU and acceptance angle $w = 180^\circ$. The different panels refer to various pointing directions: Comet nucleus direction (+z) and its opposite (-z); solar panel axis (+y); direction perpendicular to the y and z axes (+x). The average fluence collected from the nucleus direction is $1.67 \cdot 10^{12} \text{ m}^{-2}$, close to the isotropic total fluence ($1.66 \cdot 10^{12} \text{ m}^{-2}$).

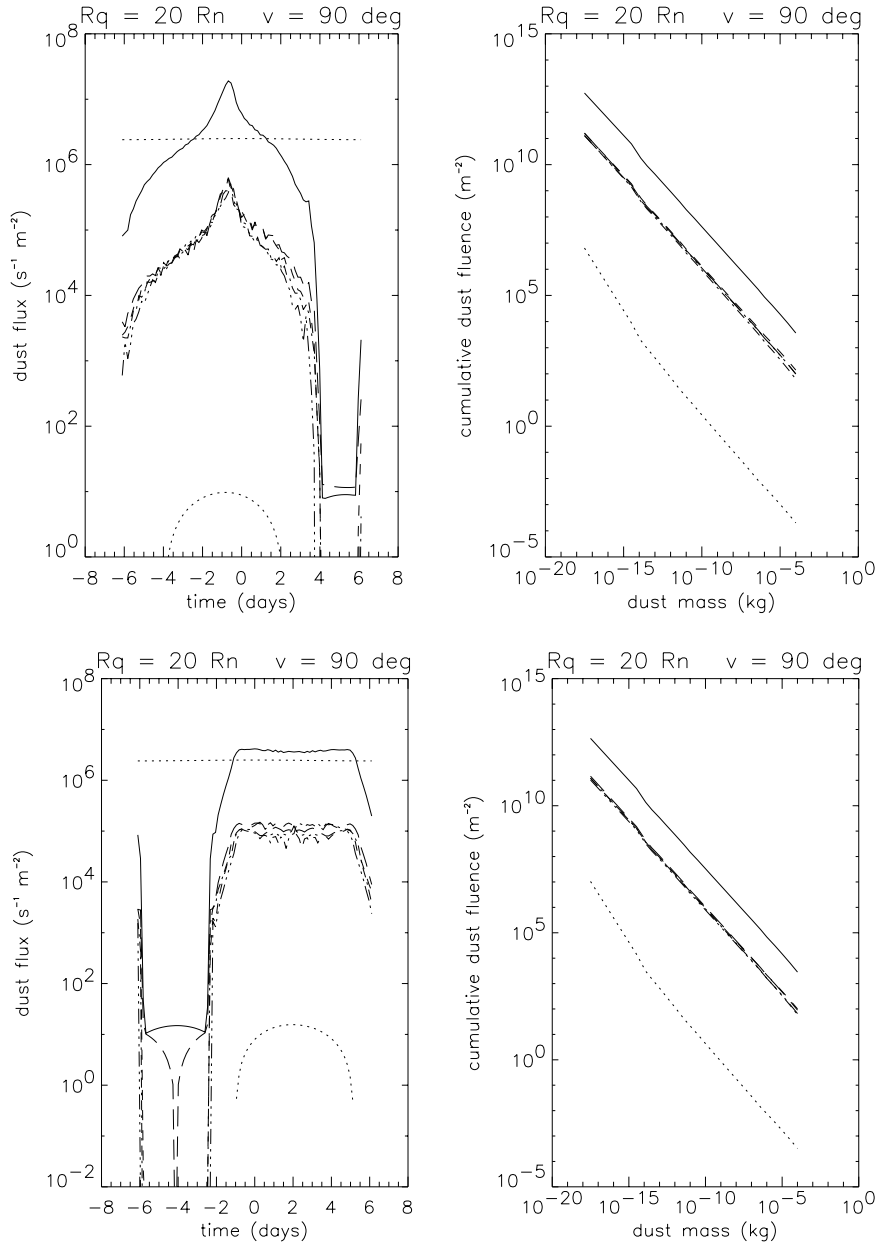


Fig. 17. Flux $\psi(t)$ (left panel) and cumulative fluence $h(m)$ (right panel) collected during a circular probe orbit with $q_p = 15$ km, $e_p = 0.01$, $\omega_p = 30^\circ$, $\Omega_p = 30^\circ$, $i_p = 30^\circ$, sun-comet distance 1.06 AU and acceptance angle $w = 180^\circ$. The different lines refer to various pointing directions: Comet nucleus direction ($+z$, continuous line) and its opposite ($-z$, lower dotted line); solar panel direction ($+y$, dot dashed line) and its opposite ($-y$, three dot and dashed line); direction perpendicular to the y and z axes ($+x$, dashed line); isotropic flux (constant upper dotted line).

Fig. 18. Flux $\psi(t)$ (left panel) and cumulative fluence $h(m)$ (right panel) collected during a circular probe orbit with $q_p = 15$ km, $e_p = 0.01$, $\omega_p = 30^\circ$, $\Omega_p = 90^\circ$, $i_p = 135^\circ$, sun-comet distance 1.06 AU and acceptance angle $w = 180^\circ$. The different lines refer to various pointing directions: Comet nucleus direction ($+z$, continuous line) and its opposite ($-z$, lower dotted line); solar panel direction ($+y$, dot dashed line) and its opposite ($-y$, three dot and dashed line); direction perpendicular to the y and z axes ($+x$, dashed line); isotropic flux (constant upper dotted line).

Fig. 17 shows the corresponding flux and cumulative fluence for an acceptance angle $w = 180^\circ$ and for an arbitrarily oriented probe orbit, which can be directly compared to Fig. 9 in order to check the changes due to the w parameter. Regarding the nucleus direction, the flux when the probe is on the sunsided coma is the same. On the contrary, due to the wider acceptance angle, the $+z$ direction is able here to collect reflected grains when the probe is in the nightside coma, so that the deep $+z$ flux minimum is deeper in Fig. 9 (no reflected grains collected) than in Fig. 17. For the same reason, the antinucleus direction is able to collect reflected grains when the probe is on the sunsided coma. All the other surfaces are dominated by reflected grains. The cumulative fluences show that the ratio of direct and reflected cumulative fluences is the same in Figs. 9 and 17. Thanks to the non radiality of the motion of direct grains, on the $+y$ and $+x$ surfaces, the

flux is dominated by direct grains, although the absolute values are reduced by the scalar product effect. As in Fig. 16, we can conclude that on these surfaces the flux of direct grains reaches 1% of that on the nucleus facing surface, a value much higher than that due to reflected grains.

These conclusions are confirmed by Figs. 18, 19 and 20, related to other probe orbit parameters.

4. Discussion

Until now, studies of the dust impacts on probes in the vicinity of a cometary nucleus have assumed a point source of dust, and, to one exception, an isotropic source. This paper provides the first study in which (1) the extended character of the source represented by the nucleus surface is taken into account, and (2) a non-spherical nucleus is considered (giving birth to an inhomogeneous

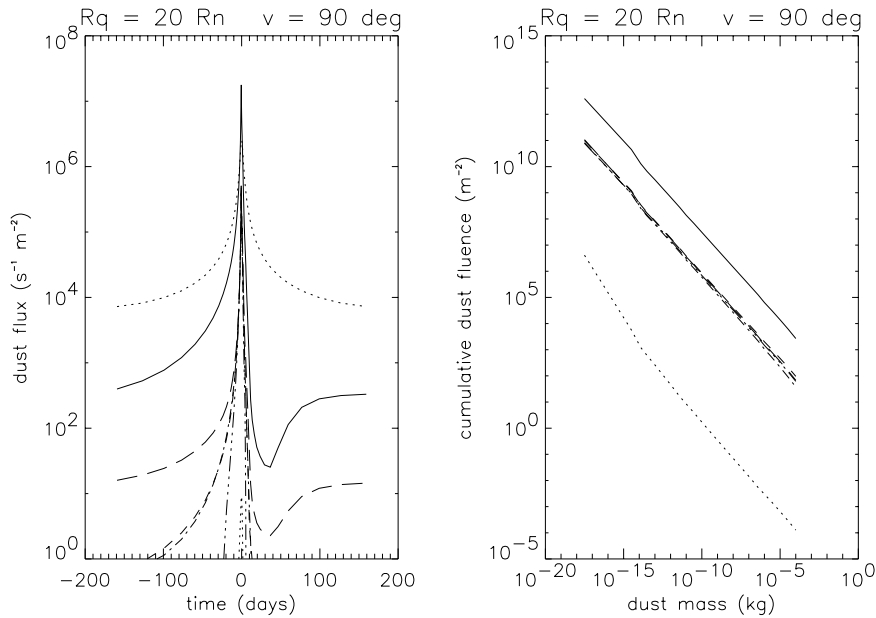


Fig. 19. Flux $\psi(t)$ (left panel) and cumulative fluence $h(m)$ (right panel) collected during a probe orbit with $q_p = 15$ km, $e_p = 0.9$, $\omega_p = 30^\circ$, $\Omega_p = 30^\circ$, $i_p = 30^\circ$, sun-comet distance 1.06 AU and acceptance angle $w = 180^\circ$. The different lines refer to various pointing directions: Comet nucleus direction (+ z , continuous line) and its opposite ($-z$, lower dotted line); solar panel direction (+ y , dot dashed line) and its opposite ($-y$, three dot and dashed line); direction perpendicular to the y and z axes (+ x , dashed line); isotropic flux (constant upper dotted line).

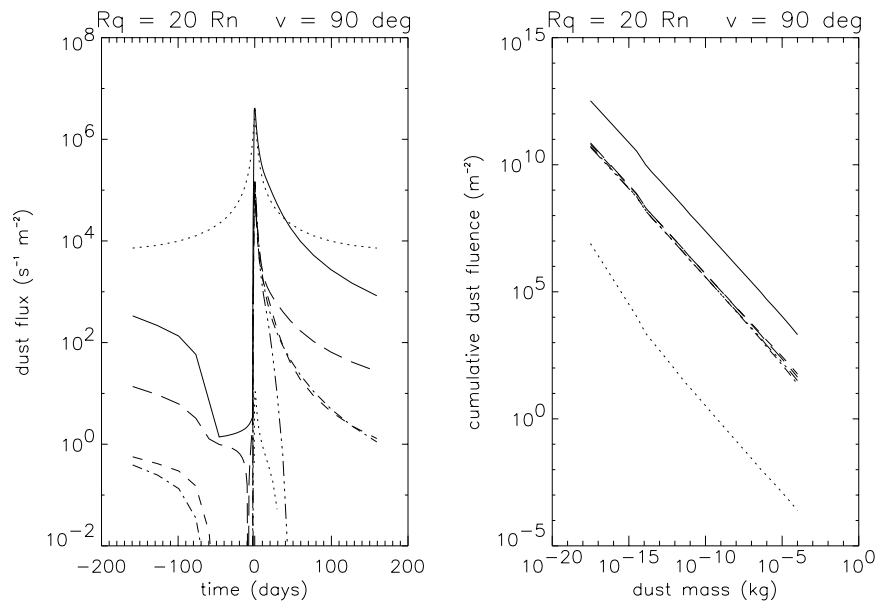


Fig. 20. Flux $\psi(t)$ (left panel) and cumulative fluence $h(m)$ (right panel) collected during a probe orbit with $q_p = 15$ km, $e_p = 0.9$, $\omega_p = 30^\circ$, $\Omega_p = 90^\circ$, $i_p = 135^\circ$, sun-comet distance 1.06 AU and acceptance angle $w = 180^\circ$. The different lines refer to various pointing directions: Comet nucleus direction (+ z , continuous line) and its opposite ($-z$, lower dotted line); solar panel direction (+ y , dot dashed line) and its opposite ($-y$, three dot and dashed line); direction perpendicular to the y and z axes (+ x , dashed line); isotropic flux (constant upper dotted line).

geneous dust coma). The numerical parameters are adapted to the future “Rosetta” mission, and the results are provided for the Rosetta orbiter axes, so that the pollution on all probe surfaces can be directly evaluated. These results provides the first evaluation of the limitations and of the validity of the isotropic flux model, since no comparison with an isotropic model was done in F97. Conversely, this comparison allows us to conclude that our present results regarding direct grains are surely free of errors due to model normalizations, because the fluence averages provided by the isotropic model and by our present dust model are perfectly consistent for all the probe orbits configurations we have taken into account.

While the average of the dust flux and fluence on the + z Rosetta axis (the nucleus direction) over the whole set of probe orbits is in perfect agreement with the isotropic model, the in-

dividual total fluence values related to the individual orbits are affected by changes up to a factor 5. This is due to the present coma anisotropy. Since the nucleus surface is assumed here perfectly homogeneous, thus building up a coma presumably characterized by the lowest possible anisotropy, this scatter in the total fluence should be a lower limit. We can conclude that isotropic models can provide total fluences which are affected by an intrinsic error of at least a factor 5, simply due to the lowest possible coma anisotropy. Furthermore, they are unable to give information on the flux changes from orbit to orbit. The changes found here confirm qualitatively the results of F97, but are much larger: they reach orders of magnitude, with an increase of a factor 10 when the probe crosses the shocks in the coma, and with decreases of many orders of magnitude in the nightside coma. This definitely confirms that isotropic models

cannot provide more than averages over the whole probe orbit: they cannot predict the dust flux on a probe orbiting in a restricted circumnuclear region. They also are unable to give a correct estimate of the flux of reflected grains, or of the fluxes affecting surfaces other than that oriented towards the nucleus.

The comparison of the results of this paper with those obtained by F97 where a point like source, much more anisotropic than the present one, was assumed, suggest to use both results to quantify the uncertainty in the poorly known ratio between the “direct” and the “reflected” fluences. However, it might be necessary to clarify first which relation the F97 model bears to the present approach, in other words: can an ab-initio model of the kind envisioned here be equivalent (for distant encounters) to an effective dust source of the kind derived in Fulle et al. (1995) and used in F97? This is essentially an unanswered question, as we now discuss.

We may ask whether the present computed dust source is compatible or not with the Giotto results, i.e., would it be possible or not to force a source of the kind compute here to the Didsy data? Note that since the range of ejection times of the grains collected by DIDSY is from hours to months, the physical significance of this question is limited, since no nucleus can be reasonably assumed three-axis stabilized over such a long period of time. Fulle et al. (1995) showed that the large grain excess of the DIDSY fluence is consistent with a power-law distribution if and only if Halley’s coma is strongly anisotropic; however, that the dust need to have a power-law spectrum is not proven; spatial anisotropy can be traded against size spectrum changes, but this also is a formal exercise without much physical significance. Finally a certain degree of coma anisotropy is required to fit the strong difference between pre and post flyby Giotto fluences, but, at the present time, this minimal amount has not yet been assessed; the coma anisotropy assumed in Fulle et al. (1995) produced in fact an excessive difference, so that future computations are needed to evaluate the best-fit anisotropy.

More fundamentally, the idea of using the fit of Fulle et al. (1995) to predict near-nucleus fluences is susceptible to the same fundamental criticism addressed to the use of outer coma gas and dust data to infer detailed properties of the nucleus and its vicinity (Crifo & Rodionov, 1998a): little information on these regions is in fact contained in the input observations, so that little conclusions are at all reachable. There is an unavoidable large arbitrariness in the derivation of the dust source of Fulle et al. (1995): the Giotto detector did only sample a segment across P/Halley’s coma which corresponds to very small space–time elements of the time–dependent Halley’s dust coma. A universal simple source law has been forced to fit these meager data, but there is after all no proof that another distribution would not perform as well or even better. There is also no guaranty that this simple fitted source would be compatible with the fluences that would have been measured in other space–time regions of P/Halley’s dust coma, if the mission had had more measuring capabilities.

In conclusion on this, it seems of little physical significance to fit extremely limited outer coma dust data with a realistic dust emission model; when near-nucleus fluences are needed, only

a statistical method whereby a set of parameters representing the possible properties of an unknown but physically plausible nucleus are varied, and the associated fluences computed, is adequate. This work is only a modest step towards it.

Returning to the comparison between F97 and the present results, it is possible that F97 thus provides an upper limit flux of reflected grains and that the comparison of the two results gives an estimate of the uncertainty range of the ratio between the reflected and the direct fluence. This ratio has an upper limit from 10^{-3} to 10^{-4} in F97, and a lower limit from 10^{-7} to 10^{-5} here. Both lower limits refer to circular orbits. For elongated ones (elliptical or petal-like), this ratio can reach 10^{-4} . The large uncertainty of these results suggests that this ratio could be used as an indirect information on the real coma anisotropy, and that the measure of the dust flux in directions different from that of the nucleus will provide useful constraints on the dust models of the coma. Due to the strong coma anisotropy they adopted, F97 found that for many favourable orbits the flux of reflected grains was higher than the direct one. With the 3D coma adopted here, this never happens. This fact further confirms that the direct/reflected fluence ratio is very sensitive to the dust environment anisotropy. The only way to collect surely reflected grains is to point collectors with tight acceptance angles (e.g. 40°) towards the present $+x$ probe axis (the $-z$ axis being forbidden, due to engineering constraints). Since the $+y$ axis is that of the solar panels, this direction will be always protected against the reflected grains if tight acceptance angles are adopted.

The non radial dust motions (induced by the coma shocks or by the boundary between the day and the night) have a fundamental effect on the dust flux on the probe surfaces which does not point to the nucleus. Surprisingly, the flux on these surface which never face the nucleus is not dominated by reflected grains, but by direct ones. In fact, the dust flux on the exposed surfaces pointing towards the $\pm x$ and $\pm y$ axes is up to 1% of the flux on the nucleus-facing surface. Since this flux is much higher than the largest possible reflected one, it can be only due to the non radial motion of direct grains. The present study thus provides the first reliable estimate of the flux on surfaces which should be maintained completely free of dust pollution, e.g. radiators, and should provide useful constraints to the construction of these devices.

The cumulative fluences (functions of the dust mass) are found to be independent from the adopted orbit. The “direct” ones are perfectly consistent with those provided by isotropic models. In other words, when the impact velocities of the collected grains will be available, it will be possible to infer the source dust size distribution starting from the cumulative fluence corresponding to the $+z$ axis. This result, in agreement with F97, is a great advantage with respect to dust experiments placed on fly–by missions, which are always heavily affected by dynamical artifacts, which mask the original size distribution (Fulle et al. 1995). On the contrary, these dynamical artifacts affect the cumulative fluence collected on the other probe axis. However, it seems that the deformations introduced by these dynamical effects do not depend on the precise probe orbit.

Unfortunately, on board the Rosetta orbiter, it is not planned to perform measurements of the cumulative fluence versus the dust mass in these directions, even though they would provide further useful observational constraints to model the source dust size distribution.

References

- Bar-Nun A., Barucci A., Bussoletti E., et al., 1993, Rosetta–Comet Rendez–vous Mission. ESA Sci. 93, 7
- Bussoletti E., et al., 1998, PASP, in press
- Crifo J.F., Itkin, A.L., Rodionov A.V., 1995, Icarus 116, 77
- Crifo J.F., Rodionov A.V., 1997a, Icarus 127, 319
- Crifo J.F., Rodionov A.V., 1997b, Icarus 129, 72
- Crifo J.F., Rodionov A.V., 1999a, Planet Space Sci. 797–826
- Crifo J.F., Rodionov A.V., 1999b, PASP, in press
- Fulle M., Sedmak G., 1988, Icarus 74, 383
- Fulle M., Colangeli L., Mennella V., Rotundi A., Bussoletti E., 1995, A&A 304, 622
- Fulle M., Colangeli L., Mennella V., Rotundi A., Bussoletti E., 1997, A&AS 126, 183
- Lamy Ph., Toth I., Jorda L., Weaver H.A., A’Hearn M.F., 1998, A&A 335, L25
- McDonnell J.A.M., Alexander W.M., Burton W.M., et al., 1987, A&A 187, 719